Natural air–sea flux of CO_2 in simulations of the NASA-GISS climate model: Sensitivity to the physical ocean model formulation

A. Romanou [a,b,*], W.W. Gregg [c], J. Romanski [d], M. Kelley [b], R. Bleck [a,b], R. Healy [d], L. Nazarenko [d], G. Russell [b], G.A. Schmidt [b,d], S. Sun [e], N. Tausnev [d]

[a] Dept. of Applied Math. and Phys., Columbia University, 2880 Broadway, New York, NY 10025, USA
[b] NASA-GISS, NY, USA
[c] NASA-GSFC, Greenbelt, MD, USA
[d] Center for Clim. Syst. Res., Columbia Univ., NY, USA
[e] NOAA/ESRL, Boulder, CO, USA

ARTICLE INFO

ABSTRACT

Results from twin control simulations of the preindustrial CO_2 gas exchange (natural flux of CO_2) between the ocean and the atmosphere are presented here using the NASA-GISS climate model, in which the same atmospheric component (modelE2) is coupled to two different ocean models, the Russell ocean model and HYCOM. Both incarnations of the GISS climate model are also coupled to the same ocean biogeochemistry module (NOBM) which estimates prognostic distributions for biotic and abiotic fields that influence the air–sea flux of CO_2. Model intercomparison is carried out at equilibrium conditions and model differences are contrasted with biases from present day climatologies. Although the models agree on the spatial patterns of the air–sea flux of CO_2, they disagree on the strength of the North Atlantic and Southern Ocean sinks mainly because of kinematic (winds) and chemistry (pCO_2) differences rather than thermodynamic (SST) ones. Biology/chemistry dissimilarities in the models stem from the different parameterizations of advective and diffusive processes, such as overturning, mixing and horizontal tracer advection and to a lesser degree from parameterizations of biogeochemical processes such as gravitational settling and sinking. The global meridional overturning circulation illustrates much of the different behavior of the biological pump in the two models, together with differences in mixed layer depth which are responsible for different SST, DIC and nutrient distributions in the two models and consequently different atmospheric feedbacks (in the wind, net heat and freshwater fluxes into the ocean).

© 2013 Elsevier Ltd. All rights reserved.

1. Introduction

Over the 20th century the ocean has taken up about 1.5–2.0 Pg C yr^{-1}, i.e. about 25–30% of all the manmade emissions of CO_2 from fossil-fuel burning, cement manufacturing and land use change (Khatiwala et al., 2009; LeQuéré et al., 2009; Sabine et al., 2004). The geographic pattern of the oceanic sink is characterized by uptake at higher latitudes and outgassing in the tropics (Takahashi et al., 2009; Gruber et al., 2009). The ocean–atmosphere CO_2 exchanges, which act on timescales of hours to days, and the deep-ocean export of carbon, which acts on timescales of days to years and longer, together with land–atmosphere exchanges, set the atmospheric CO_2 concentration and its radiative impact on Earth's climate (Friedlingstein et al., 2006). At the same time, ocean

circulation changes due to variations of the physical forcing of the ocean, such as winds and air–sea freshwater fluxes, may affect the geographical patterns of deep water formation leading to large changes in the CO_2 uptake patterns (Marinov et al., 2008b).

Several studies have emphasized the uncertainty in the estimates of the magnitude and variability of the air–sea flux of CO_2 in the Earth's climate system (LeQuéré et al., 2009; Gruber et al., 2009; Takahashi et al., 2009; Friedlingstein et al., 2006). These uncertainties mainly arise from incomplete observational coverage but also from insufficient model complexity, i.e. not realistic process simulation or lack of components, as well as model errors. For example, the interannual variability and the long-term trends in the flux of CO_2 in the atmosphere, either the natural trends or the anthropogenic trends, are affected primarily by changes in sea surface temperature (SST), surface wind and ocean pCO_2 distribution. Ocean biogeochemistry (the biological or soft-tissue pump) affects dissolved inorganic carbon (DIC) which in turn determines pCO_2. Doney et al. (2004) showed that model biases can be attributed to changes in surface forcing, subgrid-scale parameterizations

* Corresponding author at: Dept. of Applied Phys. and Applied Math., Columbia University, 2880 Broadway, New York, NY 10025, USA. Tel.: +1 212 678 5520; fax: +1 212 678 5550.
E-mail address: ar2235@columbia.edu (A. Romanou).

and model complexity, all of which affect model-ocean transport and dynamics and eventually degrade ocean tracer and carbon cycle variable distributions (e.g. air–sea CO_2 flux, anthropogenic CO_2 uptake and export production). Marinov et al. (2008a) illustrated how deep ocean ventilation determines the pathways that atmospheric CO_2 follows after uptake and how these pathways are affected by the biological pump.

Uncertainties become even more apparent in a coupled atmosphere–ocean-carbon model setting in which errors in the ocean/atmospheric background models can be amplified or diminished by the coupling and hence mask the real climate/carbon-cycle feedbacks in such models (Cox et al., 2000).

Assessing the model carbon cycle and the uncertainties associated with the representation of physical and biogeochemical processes is crucial in improving the models and subsequently the estimates of the change in air–sea carbon fluxes. The physical model describes the large-scale vertical exchanges (ventilation, convection and water mass formation, subduction) and the lateral transports (both mean and eddy induced) that affect the biogeochemistry response and ultimately the gas exchange flux to/from the atmosphere (Gnanadesikan et al., 2002; Schneider et al., 2006; Ito et al., 2010). These processes affect the distributions of preformed DIC in the ocean (Marinov et al., 2008a) as well as the upward transport of nutrients into the euphotic zone needed to sustain the marine biological production. Downward transport (export) of particulate organic matter from the upper water column to depth also changes the vertical gradient of DIC in the water column (Volk and Hoffert, 1985). Deep carbon export flux determines the efficiency with which carbon is transported to depth away from further contact with the atmosphere on long time scales (Henson et al., 2012). Variations in the export lead to changes in the air–sea CO_2 exchanges and the partitioning of carbon between the oceanic and atmospheric reservoirs (Schneider et al., 2006).

The purpose of this paper is to examine the sensitivity of the carbon uptake by the ocean to parameterizations that relate to different vertical coordinate systems, thereby assessing the uncertainty in the carbon sources/sinks distribution based on physical model differences. This is particularly interesting, albeit complex, in the context of coupled atmosphere–ocean-ice models where feedbacks may lead to error compensation or amplification in the determination of the CO_2 fluxes. Specifically, we examine the divergence in model solutions during spin up and at equilibrium of two carbon cycle climate models that share the same atmospheric, ice and ocean biogeochemistry components while differ in the ocean model component. This assessment will set the stage for a better determination of the biases in the transient, present day climate, and future climate simulations.

The paper is arranged as follows: Section 2 provides a description of the two GISS climate models with emphasis placed on the oceanic components and parameterizations therein, the biogeochemical model, the gas exchange and the radiative 3-way coupling between the ocean, the atmosphere and the biogeochemistry. Section 3 provides an overview of the external datasets used in this study. These are either observational or synthetic datasets used for forcing, initialization and model validation. In the fourth section we present the model results; firstly focusing on the physical model differences with present-day-observed climatologies in order to assess the realism of the simulations, the extent of the inter-model differences, as well as elucidate the reasons that such differences exist. The second part of the Results section describes and evaluates the carbon cycle differences between the models. This part is organized by the three major pathways carbon is distributed in the oceanic system, the solubility, biology and carbonate pumps. Finally, Section 5 summarizes the conclusions of this study.

2. Model description

Two incarnations of the GISS climate model exist coupled to prognostic ocean carbon cycle, both using the same atmospheric, land and ice components but different ocean models. Results from these runs have been submitted to the Coupled Model Intercomparison Project Phase 5 (CMIP5; http://cmip-pcmdi.llnl.gov/cmip5/) as GISS-E2-R-CC and GISS-E2-H-CC which are the carbon cycle (CC) versions of modelE2 coupled to the Russell (R) or Hycom (H) oceans. In this paper, we will be using the abbreviations GISSER and GISSEH to refer to GISS-E2-R-CC and GISS-E2-H-CC respectively. A description of each component is provided below, with the emphasis placed mainly on the carbon model and the differences between the two ocean models.

2.1. The atmospheric model, modelE2

ModelE2 is an updated version of the GISS atmospheric model (modelE) that was included in the Climate Model Intercomparison Project (CMIP3) (and IPCC 4th Assessment Report) simulations (Schmidt et al., 2006; Hansen et al., 2007) and which is currently used in the CMIP5 experiments (Schmidt et al., 2012).

Improvements include (a) a finer horizontal resolution, at 2 by 2.5° latitude/longitude and 40 levels in the vertical with the top of the atmosphere at 0.1 mb, (b) refinements in the cloud microphysics, (b) a new turbulence scheme with no dry convection, (c) a new gravity wave drag parameterization, (d) new glacial-melt and melt-pond fraction and (e) updated radiative transfer, aerosol and ozone input datasets. Model time steps are about 4 min for the core dynamics, 30 min for the model physics and 2.5 h for radiative calculations in order to reduce computational costs. The model employs a quadratic upstream differencing scheme for the advection of tracers such as CO_2 that is very accurate and non-diffusive (Prather, 1986).

2.2. The ocean models

ModelE2 is coupled to two different coarse-mesh ocean models, either to the Russell Ocean model (GISSER) or to HYCOM (GISSEH). The two ocean models differ mainly in the representation of the vertical coordinate which has important implications for estimating mixing, ventilation and the representation of eddies therein. Using these two distinct models interchangeably aims to elucidate and better assess the sensitivity of the carbon storage in the ocean to two numerical representations of the ocean circulation. This capability enables us to estimate and address uncertainties in the simulated climate due to different ocean physics parameterizations. Details in the two ocean models are given below.

2.2.1. The Russell ocean model

The Russell ocean model (Russell et al., 1995; Hansen et al., 2007) is a non-Boussinesq mass-conserving ocean model with 32 vertical levels and $1 \times 1.25°$ horizontal resolution. All terms are solved on an Arakawa C-grid except the Coriolis term that is solved on a D-grid. The vertical coordinate is a stretched z-level coordinate (sometimes described as z^*) and has a free surface and natural surface boundary fluxes of freshwater and heat. It uses the Gent and McWilliams (1990) scheme for isopycnal eddy fluxes and isopycnal thickness diffusion which is known to lead to weaker and more realistic convective mixing, particularly in the Southern Ocean. Vertical mixing is parameterized by the K-Profile Parameterization (KPP) vertical mixing scheme (Large et al., 1994) with non-local mixing effects included. Vertical advection is discretized using a centered differencing scheme. Interactions of ocean with other model components as well as tracer advection are done at

15 min intervals while the timestep for the model dynamics is 3.75 min. In this simulation the Bering strait is 3 grid points wide.

2.2.2. The HYCOM

The Hybrid Coordinate Ocean Model (HYCOM) is the hybrid version of the Miami Isopycnal Coordinate Ocean Model (MICOM; Bleck et al., 1992) and it is described in Sun and Bleck (2006) variant C. It uses p coordinates near the surface and isopycnals in the ocean interior. The version used here has a horizontal resolution of $1 \times 1 cos\phi$, where ϕ is the latitude and 26 coordinate layers, a bipolar grid of matching resolution north of 60°N and an open Bering Strait and increased eddy diffusivity. Within 10° north and south of the equator, the latitudinal resolution is increased up to 0.03° at the equator.

Each coordinate layer is isopycnal and is assigned a "target" density which it follows throughout the ocean except where the target isopycnal outcrops. At low latitudes the vertical layers are isopycnal in character but become constant-depth layers poleward. The hybrid coordinate system therefore maintains vertical resolution in unstratified water columns, such as in the mixed

Table 1

Synopsis of Russell and HYCOM ocean model parameters that are relevant to vertical mixing.

	GISSER	GISSEH
Atmos-ocean interact. step	30 min	30 min
Tracer adv. timestep	15 min	12 h
Vert. diff. coeff (KPP)	$1e{-}5$ m²/s	$3e{-}7$ m²/s
Vert. visc. coeff (KPP)	$1e{-}4$ m²/s	$5e{-}5$ m²/s
Fraction of BL where solar rad. is absorbed	1	Variable, based on Jerlov
Depth of KPP	To the bottom of water column	To the bottom of mixed layer
Critical Richardson number	0.3	0.45

layer and also in shallow regions. Judicious choice of target values allows the near-surface part of the ocean to always be represented by fixed-depth layers.

A combination of two schemes is used for vertical mixing. In the turbulent surface mixed layer, the mixing scheme is KPP (Large et al., 1994) with non-local mixing effects included. Beneath the mixed layer, a mixing scheme specifically designed for isopycnic
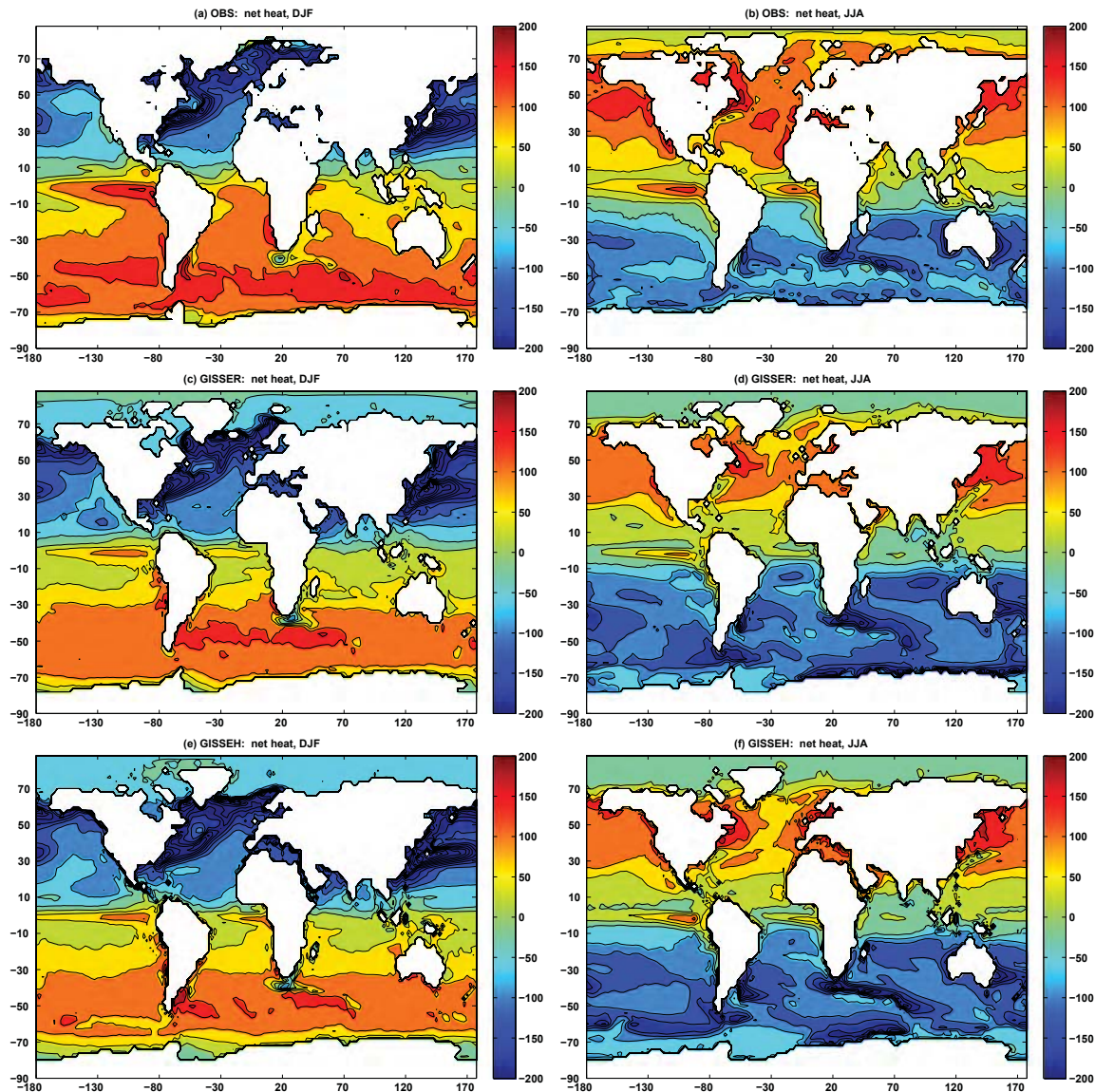

Fig. 1. Net heat flux (in W m^{-2}) climatology and model differences during December–January–February (DJF) and June–July–August (JJA). (a) and (b) observations (OAFLUX data), (c) and (d) GISSER and (e) and (f) GISSEH. Positive values mean flux into the ocean.

coordinate models (McDougall and Dewar, 1998) is used. In the latter, diapycnal diffusivity depends on the smaller of two numbers: a constant diffusivity of 2×10^5 m²/s and a stratification-dependent diffusivity after Gargett (1984). For the tracers, there is no isopycnal diffusion. Deep convection at high latitudes is parameterized through a convective adjustment scheme. Brine rejected during freezing is uniformly distributed in the uppermost 200 m if the depth is greater than 1000 m or the total water column depth otherwise. The coefficient of the lateral T/S diffusion is enhanced near the equator in order to resolve tropical instability waves which are known to be highly diffusive. The Gent–McWilliams scheme for parameterizing the effect of baroclinic instability is included via direct isopycnal interface smoothing and is limited to the isopycnic coordinate domain (which excludes the near-surface waters).

The time integration is based on the split-timestep method (Bleck and Smith, 1990) in which the barotropic timestep is 50 s for the faster modes while the baroclinic time step is half hour. The coupling with the atmosphere is synchronous. Tracer transport takes place once every 12 h.

Table 1 shows some of the key parameters in the two ocean models used here. More details on the physical ocean models can be found in Schmidt et al. (2012) as well.

2.3. The ocean biogeochemistry model, NOBM

The interactive ocean carbon cycle model consists of a biogeochemical model (NASA Ocean Biogeochemistry Model, NOBM, Gregg and Casey, 2007) and a gas exchange parameterization for the computation of the CO_2 flux between the ocean and the atmosphere.

NOBM utilizes ocean temperature and salinity, mixed layer depth and the ocean circulation fields and the horizontal advection and vertical mixing schemes obtained from the host ocean model (Russell or HYCOM) as well as shortwave radiation (direct and diffuse) and surface wind speed obtained from the atmospheric model to produce horizontal and vertical distributions of several biogeochemical constituents.

The abiotic constituents of NOBM (nutrients and carbon) are conservative and both biotic and abiotic components are subject to different dynamical interactions. There are four phytoplankton groups (diatoms, chlorophytes, cyanobacteria, and coccolithophores), which have distinct maximum growth rates, sinking rates, nutrient requirements, and optical properties, in order to represent the huge variety of physical and biological environments occurring in the global ocean. Four nutrients (nitrate, silicate, ammonium and iron), three detrital pools (for nitrates/carbon, silicate and iron) and a single herbivore component are also represented. The carbon submodel parameterizes the cycling of carbon through the phytoplankton, herbivore and detrital components, affecting the dissolved inorganic and organic carbon in the ocean and interacting with the atmosphere. The local profiles of underwater irradiance are computed bia a radiative transfer calculation and are needed to compute the growth of the phytoplankton groups, their sinking profiles due to biologically mediated absorption and scattering in the water column. These radiative calculations which depend on the spectral nature of the irradiance are based on laboratory experiments of the optical properties of phytoplankton groups (Gregg and Conkright, 2002).

Particle export in NOBM is represented by gravitational settling (sinking). Sinking of particles is variable for the phytoplankton groups and detrital components. The corresponding sinking rates are derived from mean size estimates for the phytoplankton groups, and detritus is adjusted to meet the global distribution of nutrients. The values are shown in Table 2. The sinking rate is specified for 31 °C and is adjusted for viscosity using Stokes Law (Csan-

ady, 1986), with temperature parameterization (Gregg and Casey, 2007; Gregg et al., 2012).

NOBM has been used previously to understand and evaluate the nature of seasonal variability of total chlorophyll, the phytoplankton functional group and the nutrient distributions in the global oceans (Gregg and Casey, 2007) and has been validated extensively against in situ and satellite observations (Gregg et al., 2003a).

2.4. The air–sea gas exchange

The air–sea gas transfer of CO_2 is parameterized as

$$F = k_w \alpha([CO_2] - [CO_2]_{sat}) \qquad (1)$$

where F is the flux of CO_2 in/out of the ocean, kw is the gas transfer velocity for CO_2, α is the solubility, a function of pressure, SST and SSS, and $[CO_2]$ is the surface ocean concentration of CO_2. $[CO_2]_{sat}$ is the corresponding saturation concentration of CO_2 in equilibrium with a water–vapor-saturated atmosphere at a total atmospheric pressure P and a given atmospheric pCO₂ level:

$$[CO_2]_{sat} = \frac{P}{P^0}[CO_2]^0 \qquad (2)$$

where $P^0 = 1$ atm and $[CO_2]^0$ is the saturation concentration at 1 atm total pressure.

The gas transfer velocity is given by,

$$k_w = c\left(\frac{Sc}{660}\right)^{-1/2} u^2 \qquad (3)$$

where u is the surface wind speed and c is the piston velocity coefficient taken here equal to $0.337/(3.6 \times 10^5)$. The value of c has been agreed upon by the Ocean Carbon Model Intercomparison Project, phase II (OCMIP-II) so that the global, annual mean gas transfer coefficient for carbon dioxide ($k_w\alpha$) is equal to 0.061 mol/m²/yr/ µatm for preindustrial times. This estimate is based on $k_w\alpha pCO_2 = 17 \pm 4$ mol/m²/yr estimated by Broecker et al. (1986) based on the global bomb radiocarbon budget divided by the preindustrial pCO₂ of 280 µatm. Sc, the Schmidt number, is computed using the temperature of the host ocean model following Wanninkhof (1992). k_w is computed only over open water. The solubility of CO_2 in the water α is also parameterized based on OCMIP using prognostic temperature, salinity and sea level pressure.

In the present set of runs atmospheric concentration of CO_2 is held constant at a global average of 285.2 ppmv, although regionally atmospheric CO_2 is allowed to vary due to the distributions of the ocean sources and sinks. In addition, air–sea CO_2 is treated as radiatively inactive and therefore air–sea ocean CO_2 exchanges do not induce any climate change.

2.5. Radiative coupling of ocean and atmosphere

In contrast to Gregg and Casey (2007), in the present model, NOBM is coupled prognostically to the atmospheric radiation module which is part of modelE2. Direct and diffuse sunlight in 6 wavebands (5 in the near IR and 1 in the visible part of the spectrum) computed by the radiation module are decomposed into the 33 wavelengths (250–3700 nm) needed for the absorption and scattering by the different phytoplankton species. The decomposition is based on the fractions of direct (diffuse) sunlight at the equator and each wavelength to the total radiation in each waveband derived from a monthly climatology provided by the Ocean–Atmosphere Spectral Irradiance Model (OASIM) and forced by MODIS data for aerosols and clouds (Gregg and Casey, 2009).
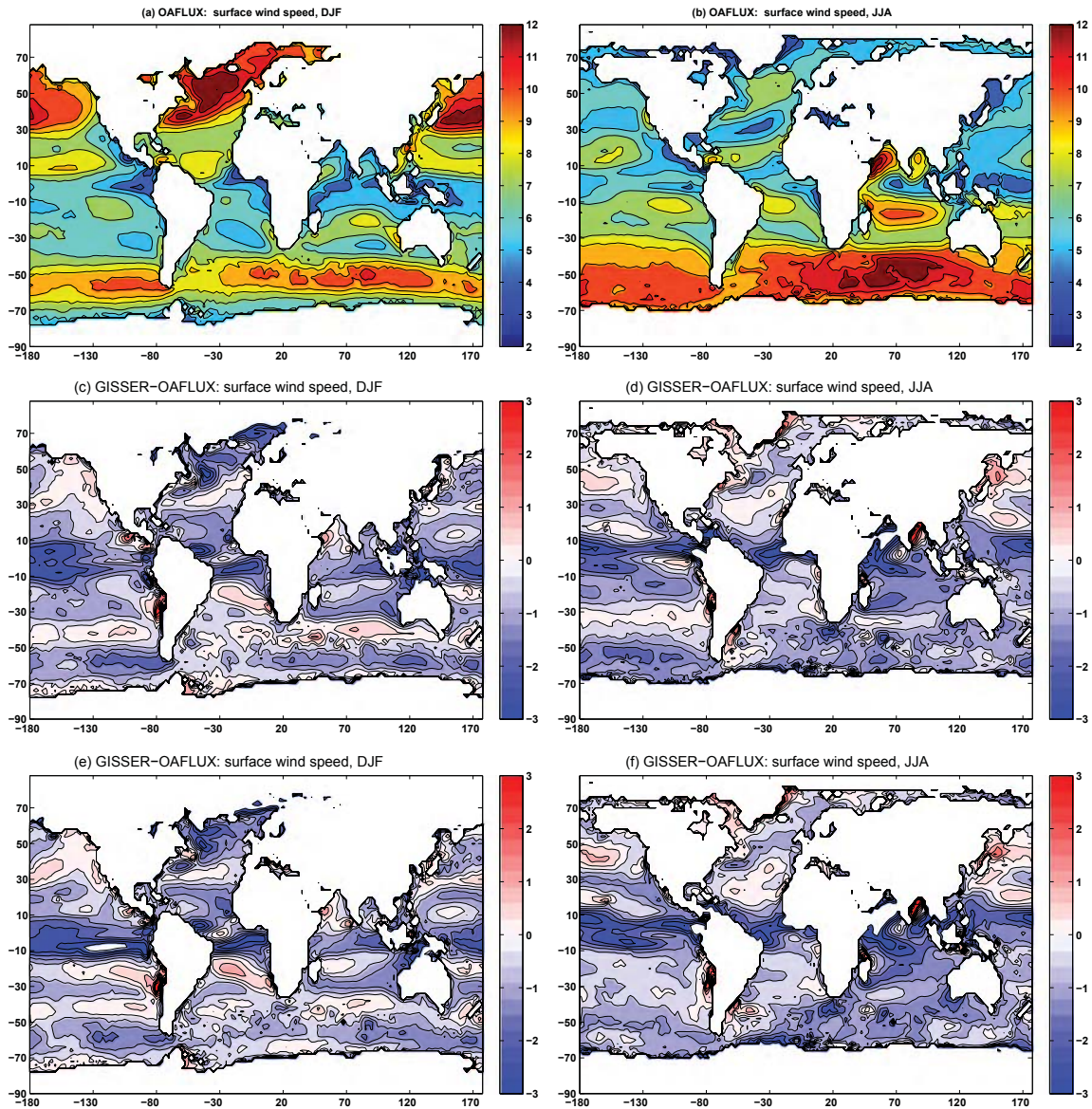
Fig. 2. Surface wind speed (m s^{-1}) climatology and model biases with respect to OAFLUX. (a) and (b) DJF and JJA climatologies from OAFLUX, (c) and (d) GISSER bias in DJF and JJA, (e) and (f) GISSEH bias in DJF and JJA.

3. Initialization/evaluation datasets

3.1. Partial CO$_2$ pressure in the ocean

Model estimated pCO$_2$ in the water, the air–sea flux of CO$_2$, solubility and piston velocity are compared to the Takahashi atlas (Takahashi et al., 2009; Takahashi, 2009) which consists of climatological mean distributions over the global oceans in non-El Niño conditions at 4×5 resolution for the reference year 2000. The Takahashi atlas is based on pCO$_2$ measurements obtained from 1970 to 2007, and utilizes SST and SSS data from the World Ocean Circulation Experiment (WOCE) cruises and wind speed data from the 1979–2005 NCEP-DOE AMIP-II Reanalysis. Piston velocity is parameterized as a function of the square of the wind speed with a scaling factor of 0.26 for long-term (monthly) mean gas transfer. Wanninkhof DSR-II (2007) suggest a transfer coefficient of about 0.36 relevant to high-frequency gas exchange. In this work, we use a value of 0.26 for the transfer coefficient for consistency with

previous model evaluation studies based on OCMIP-II parameterizations although perhaps Wanninkhof's latest estimate would be more appropriate in a coupled model context where coupling is synchronous and shorter rather than longer time scales affect the flux. The uncertainties in the Takahashi atlas are estimated at 30% and are higher than the long term mean.

Data from the study areas/stations such as the Bermuda Atlantic Timeseries Study (BATS, ftp://ftp.bios.edu/BATS), the Hawaii Ocean Timeseries Study (HOTS, Dore et al., 2009) and CARIOCA (http://www.imars.usf.edu/CAR/index.html) are also used for the validation of the seasonal cycle of pCO$_2$ in the models.

We note that, the comparison with the Takahashi atlas is used here only qualitatively to depict the spatial patterns of pCO$_2$ in the ocean. For the purposes of this paper, the Takahashi atlas is not an exact validation tool, since the model runs described here refer to a preindustrial atmosphere, in contrast to the Takahashi atlas which describes the state of ocean surface pCO$_2$ for atmospheric concentrations in year 2000.

3.2. DIC

Initial distributions of the dissolved inorganic carbon are taken from the Global Ocean Data Analysis Project (GLODAP). These distributions are the result of a synthesis of approximately 8 yr of data (1990–1998) from the global CO_2 survey that included 50 individual cruises. The data were unified into an internally consistent dataset (Key et al., 2004).

In particular, for the preindustrial spinup and the equilibrium runs described here, estimates of the preindustrial (i.e. present day – anthropogenic) distributions of DIC were used. Deviations of model results at equilibrium from the GLODAP data are useful in explaining the different way processes are resolved in the two models.

3.3. Nutrients, SST, SSS, mixed layer depths

Nutrients (nitrates and silicates) initial conditions, and SST and SSS evaluation datasets are obtained from the National Oceano-graphic Data Center (NODC) World Ocean Atlas 2005 (Locarnini et al., 2006; Antonov et al., 2006; Garcia et al., 2006). These data are provided in a monthly mean climatology at 1° resolution and 33 nominal depths and are interpolated to each ocean model's horizontal and vertical grid.

Model mixed layer depths are evaluated against a 2° global climatology which is constructed using individual T, S profiles and a combination of the critical difference values for temperature and density from the surface value, $\delta T = 0.2 \,^{\circ}C$ or $\delta \rho = 0.03 \, kg \, m^{-3}$ (deBoyer Montégut et al., 2004).

3.4. Dust-iron

Following Gregg et al. (2003b), the dust-iron deposition flux is obtained from the Georgia Institute of Technology/Goddard Global Ozone Chemistry Aerosol Radiation and Transport climatology for the period 1982–2000, except for the 1997–1999 period when data was unavailable (GOCART; Ginoux et al., 2001). The iron content is assumed to vary within each dust size class, with clay containing
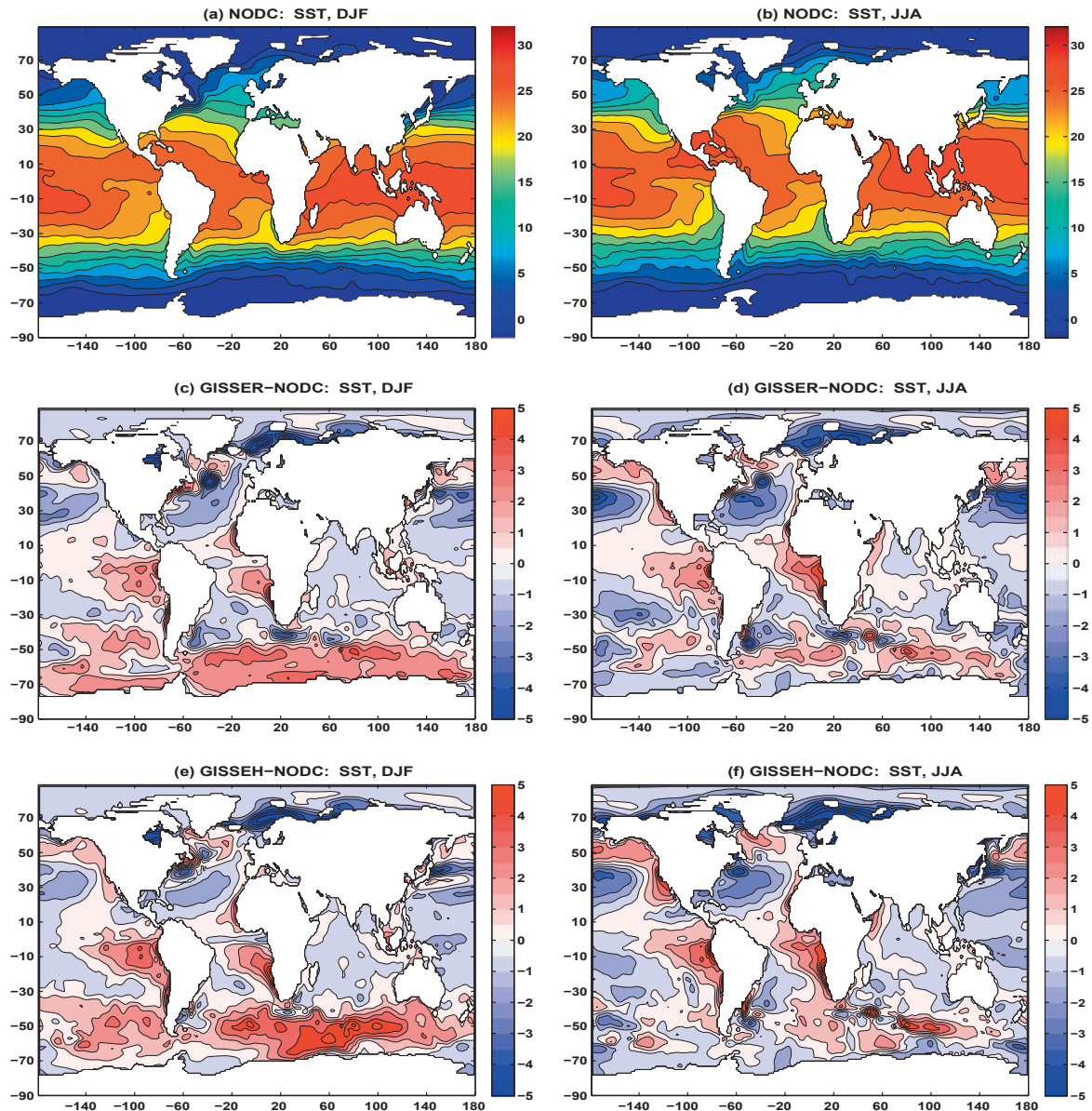

Fig. 3. Sea surface temperature climatologies (°C) from NODC and model biases. (a) DJF SST from NODC, (b) JJA SST from NODC, (c) and (d) GISSER biases from NODC during DJF and JJA respectively and (e) and (f) GISSEH biases from NODC during DJF and JJA respectively.

3.5% iron and silt containing 1.2% iron (Fung et al., 2000). Furthermore, a constant iron solubility of 2% is also assumed.

3.5. Surface radiative and thermal fluxes and surface wind speed

Surface radiative fluxes (shortwave and longwave) are obtained from the International Satellite Cloud Climatology Project (ISCCP) FD flux dataset. The resolution is 3 h at 2.5° covering July 1983 through December 2007 (see Zhang et al., 2004 for details and references). Uncertainties of the monthly fluxes are estimated to be in the range of 10–15 W m^{-2} at the surface.

Latent and sensible heat fluxes come from the Woods Hole Oceanographic Institute (WHOI) Objectively Analyzed air–sea Heat Fluxes (OAFlux) surface heat flux dataset and are used here for model evaluation. The daily data cover the period 1985 to 2009, while the monthly fluxes are available from 1958 onward. OAFlux is a blended dataset created by combining satellite-derived observations of meteorological variables with those from numerical weather prediction (NWP) model output. Comparison to in situ flux measurements shows that the mean average of the differences

between OAFlux and buoys over 107 locations (a measure of bias) is 1.0 W m^{-2}, and that the absolute mean average of the OAFlux-buoy differences (a measure of variance) is 7.4 W m^{-2}. For further information, see Yu et al. (2008).

4. Results

In the results presented below, all runs start from equilibrium conditions obtained after about 3000 yr of integration of the coupled atmosphere–ocean-ice models. The upper ocean is in statistical steady state with respect to all thermodynamic variables whereas the deeper ocean is still evolving, albeit very slowly and on timescales longer than the ones of interest here. Both models are then coupled to NOBM, using initial conditions for nutrients from NODC and Fung et al. (2000) and DIC from the GLODAP pre-industrial estimate (Key et al., 2004). Regional variations due to the ocean–atmosphere flux are computed at each grid point but the global average atmospheric CO$_2$ concentration is held constant at 285.2 ppmv. The models are further integrated until the CO$_2$ flux at the surface of the ocean is in statistical steady state and approx-
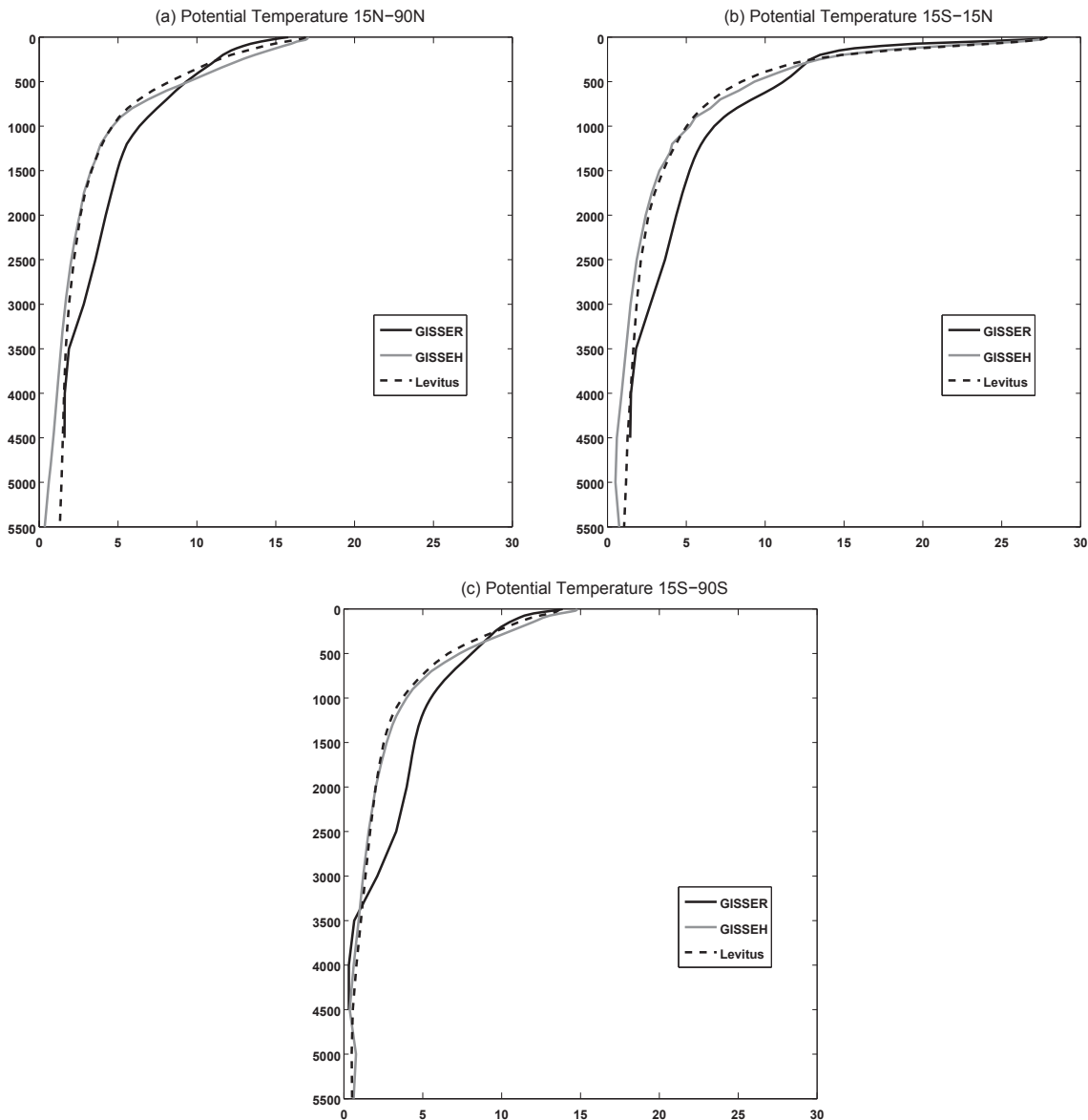

Fig. 4. Potential temperature profiles (°C) averaged over latitude zones, from the two models and the NODC data. (a) 15–90° N, (b) 15° S–15° N and (c) 15–90° S.

imately 0.9 Pg Cyr^{-1}. This corresponds to an additional 300 yr of integration after which each coupled ocean–atmosphere-biogeochemistry model is in equilibrium.

In the following discussion, observations are used only as a benchmark to assess the magnitude and realism of the intermodel differences, since observations refer to present day climate conditions whereas models simulate here an unperturbed, stable, preindustrial climate.

4.1. Physical ocean model differences

Surface heating (i.e. the sum of radiative and thermal surface fluxes into the ocean) is shown in Fig. 1. Both model estimates agree well with the observed seasonal cycle and the inter-hemispheric differences but exaggerate the seasonal cycle amplitude (Fig. 1). In the subtropics and midlatitudes of each hemisphere, the models overestimate heat losses during the cold season (e.g. December–January–February (DJF) for the Northern Hemisphere and June–July–August (JJA) for the Southern Hemisphere) and

underestimate the heat uptake during the warm seasons. In the tropics, both models show weaker than observed heat gain during both seasons (Fig. 1), with the eastern Equatorial Pacific and the tropical Atlantic receiving about 50–100 W m^{-2} less than what OA-FLUX shows. The Pacific cold tongue region is weaker and narrower in both models compared to observations.

The model differences in surface heating patterns are related to clouds, sea-ice thickness and extent as well as the SST distributions. Both models overestimate cloud amount over the tropical regions by about 30–50% (Schmidt et al., 2012) resulting in reduced heat reaching the surface there. The models also overestimate the wintertime (DJF) cloud amount over the Arctic Ocean (Schmidt et al., 2012) thereby limiting the amount of surface cooling. In the Southern Ocean, though, during the austral winter (JJA) both models underpredict cloud cover, which leads to extreme (about 200 W m^{-2}) heat losses near the coast of Antarctica.

Surface winds are weaker in the GISS models by about 1–3 m s^{-1} (Fig. 2(a)–(d)) compared to the OAFLUX data, with the larger differences exhibited by the GISSER model. The tropical regions
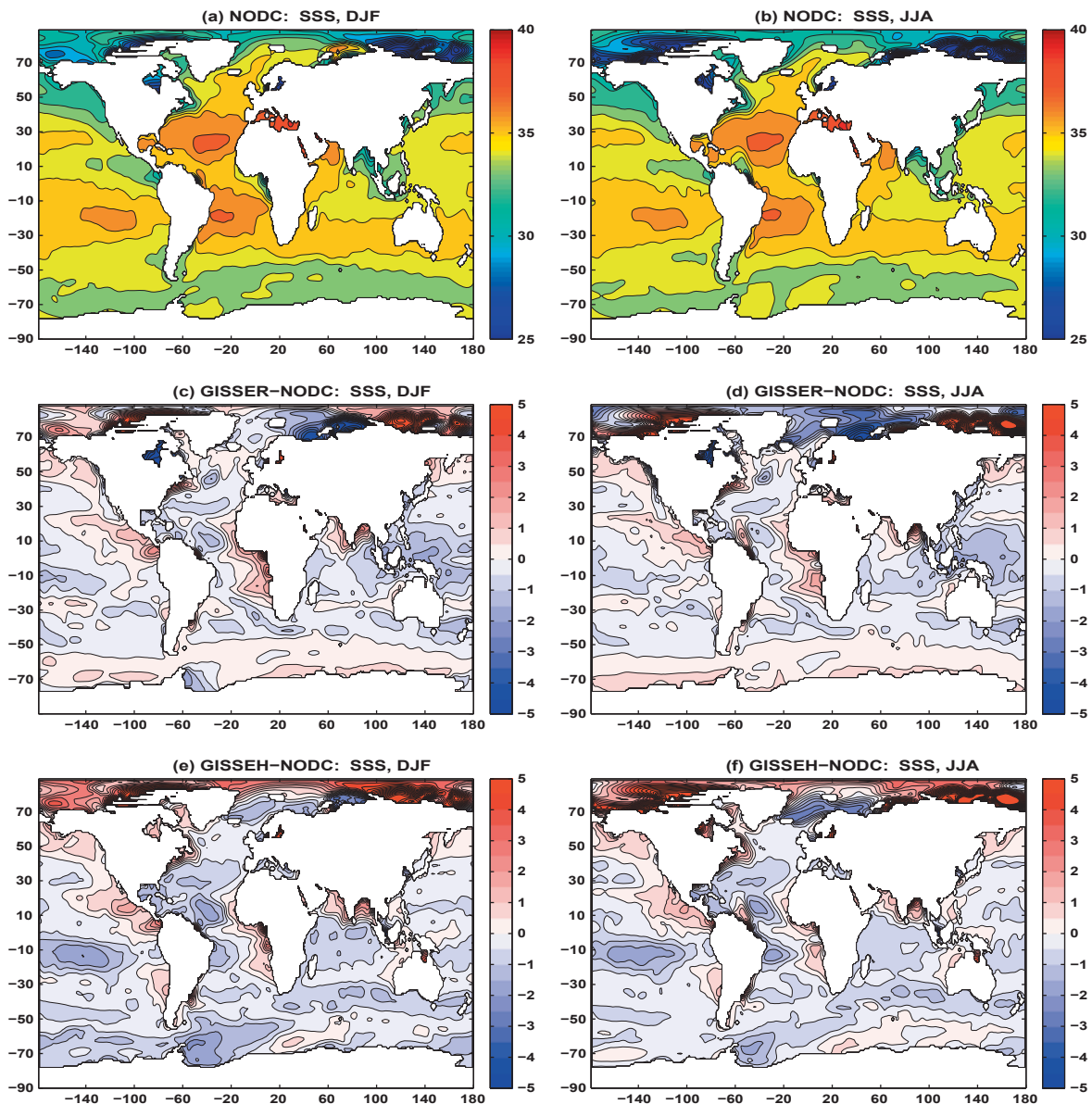

Fig. 5. Surface salinity climatology from NODC and model differences. (a) and (b) SSS from NODC for DJF and JJA respectively, (c) and (d) SSS biases in GISSER for DJF and JJA respectively and (e) and (f) SSS biases in GISSEH for DJF and JJA respectively.

as well as the wintertime storm tracks (in the northwest Atlantic and Pacific Oceans and in the Southern Oceans) are the regions where the largest underestimates exist. In contrast, both models overpredict the coastal winds along the western continental borders during both DJF and JJA, due to the inability of the low resolution grid to resolve steep topography there.

As a result, surface temperature is about 2–4 °C warmer than observations in both models in the Southern Ocean, with the larger overestimates displayed by GISSEH during the warm season (DJF, Fig. 3). These differences are explained by the lack of cloudiness that allows more heating to reach the surface, increasing the thermal stratification near the surface, further inhibiting vertical exchanges which would otherwise cool the surface. In the Northern Hemisphere, the colder wintertime SSTs are linked to increased heat losses due to the decreased cloudiness. In the tropics, the much warmer surface ocean in the models, which is due to ocean model deficiencies, is compounded by the increased clouds which prevent radiative cooling of the ocean surface.

Zonally averaged potential temperature vertical profiles (Fig. 4) reveal how model differences are transferred to the deeper ocean

levels. In the 3 regions depicted (Northern Hemisphere extratropics, tropics and Southern Hemisphere extratropics), model estimates bracket the observations down to about 200 m, with GISSER being colder than the observations and GISSEH. Between 200 m and 3500 m depth, GISSER temperatures are much warmer than both observations and HYCOM (Fig. 4). Such mid-depth warming in GISSER is a result of the excessive warming of the surface ocean in the deep convection regions, which forms waters that ventilate the mid-ocean depths with warm biases (seen in Fig. 3).

Surface salinity differs significantly between the two models and from observations particularly in the Arctic Ocean (Fig. 5). Large overestimates exist there because of increased brine rejection during excessive ice formation in DJF as well as due to deficient freshwater river outflow (Schmidt et al., 2012). In the summer months (JJA) in the Arctic Ocean both models underpredict the sea ice coverage, which implies excessive melting of the wintertime sea ice leading to lower surface salinity. In the Southern Ocean, GISSER overestimates sea surface salinity compared to GISSEH, because of the larger evaporation in that model (Fig. 6). Surface salinity is also overestimated in the models at the coastal
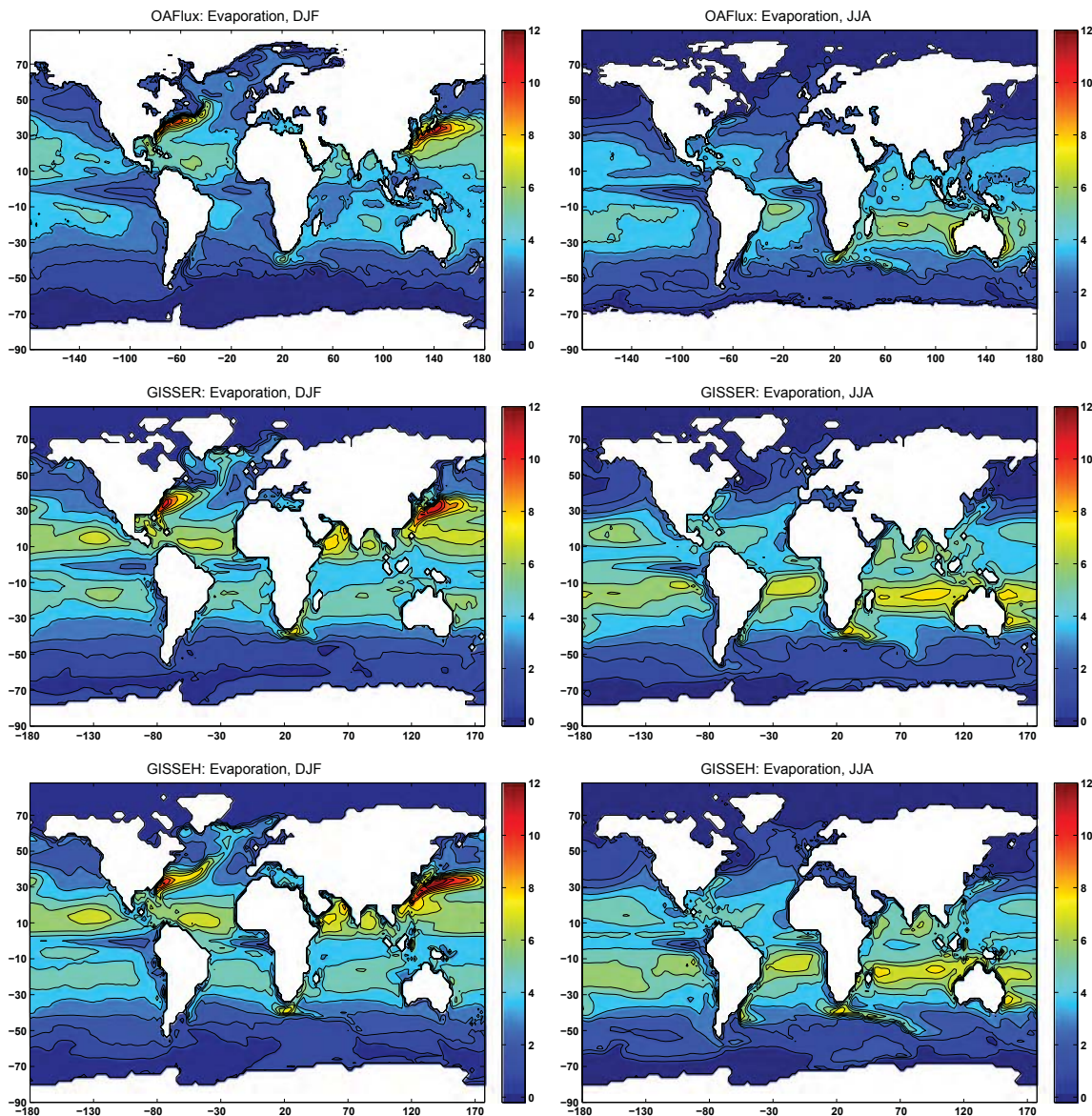

Fig. 6. Evaporation (in W m^{-2}) climatologies from observations and the two model runs for DJF (left columns) and JJA (right columns).

upwelling regions again due to excessive evaporation in these regions, more clouds and warmer SSTs. Weaker than observed coastal winds impose limited upwelling, drawing to the surface warmer water from shallower depths, thereby enhancing evaporation and leading to increased SSS distributions.

Elsewhere in the tropics and in the subtropics, slightly lower than observed model surface salinities are attributed to the increased model precipitation compared to GPCP climatology (Schmidt et al., 2012) which exceeds observations in the tropics by about 2–10 mm d^{-1} and the subtropics by 1–2 mm d^{-1}.

Mixed layer depths (MLDs) are shallower than observed in the Southern Ocean in both models, especially in GISSEH (Fig. 7). Deep convection in the North Atlantic reaches greater depths in GISSEH but is confined in a smaller geographical region in the models than in the observations, leading to a decreased mid-depth warming bias in GISSEH (Fig. 4), and therefore more realistic deep ocean temperature profiles than GISSER. During JJA, wintertime mixed layer depths against the Antarctic coast are deeper than observed in GISSER due to reduced cloudiness and too little sea-ice, excessive cooling and dense water formation. By contrast, in the Arctic Ocean, winter mixed layer depths in both models are shallower than observed due to the insulating effect of too much model ice.

4.2. The air–sea surface CO_2 flux: solubility pump differences

During spinup, both ocean models emit CO_2 to the atmosphere for an adjustment period of about 250 yr, implying that the oceanic initial condition has too much surface DIC and is out-of-balance with the model atmosphere. The rearrangement of DIC within the mixed layer, together with the slow evolution of deep ocean properties are responsible for this adjustment period, since sea surface temperature, surface winds or mixed layer depth are in statistical steady state while the air–sea CO_2 flux is not interactive with the model's radiation and does not affect the model climate.

The spatial distribution of the CO_2 flux in the two models at equilibrium for a climatological December–January–February (DJF) and June–July–August (JJA) is shown in Fig. 8, together with the distribution of the flux from the Takahashi atlas. Both models predict a strong sink of CO_2 in the cold season hemisphere. During DJF, the North Atlantic deep convection region (Labrador Sea, Ice-
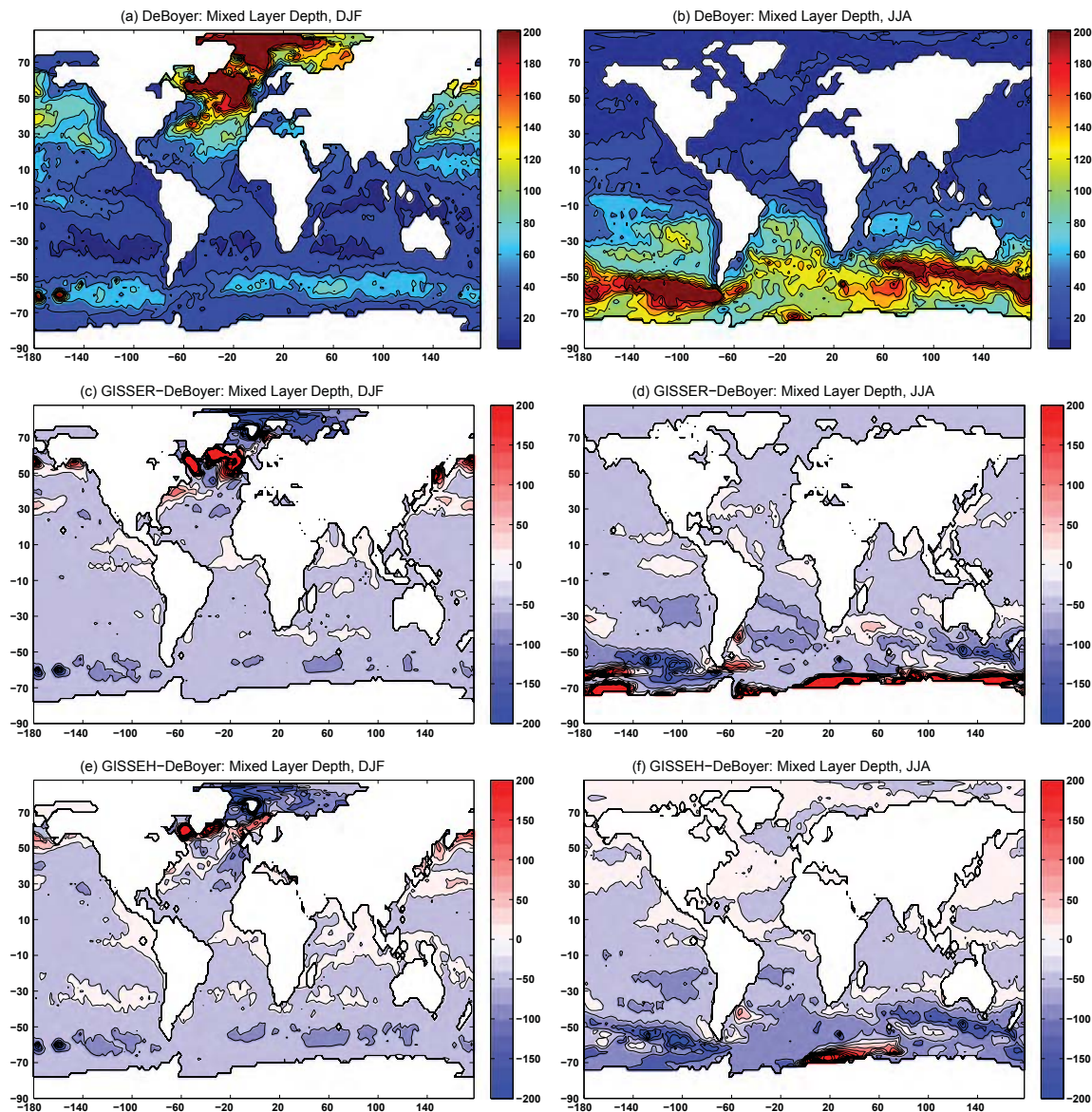

Fig. 7. Mixed layer depths climatologies (in m) from (a) and (b) the deBoyer atlas, (c) and (d) GISSER and (e) and (f) GISSEH for DJF and JJA.

land and Norwegian basins) dominates the global CO_2 drawdown (Fig. 8(c) and (e)) which is more pronounced in GISSEH than in GIS-SER. The maximum drawdown in the N. Atlantic sink region is about 8 mol CO_2 m^{-2} yr^{-1} in GISSER and about 6 mol CO_2 m^{-2} yr^{-1} in GISSEH although the latter over a more extended area. As shown in the previous section, DJF SSTs are warmer by about 5 °C in GIS-SEH than GISSER (Fig. 8(c) and (e)) therefore SST does not drive the more vigorous uptake in GISSEH. Storm tracks, on the other hand, are stronger in GISSEH than in GISSER (Fig. 2(c) and (e)) by about 1–2 m s^{-1} on the monthly mean which partly explains the stronger CO_2 sink in this model. At the same time, surface ocean pCO_2 in GISSEH is lower (Fig. 9) which further enhances the CO_2 uptake by the GISSEH ocean moreso than the GISSER ocean. It is therefore the dependency of the flux (Eqs. (1)–(3)) on the surface pCO_2 and the surface wind speeds that mainly determines the uptake in the North Atlantic rather than the SST field in these two models.

During JJA, the North Atlantic remains a sink region of CO_2, although a little weakened in magnitude because the storm tracks are weaker (Fig. 8(d) and (f)). Additionally, the ocean between 20°S

and 50°S becomes a major carbon sink (Fig. 8(d) and (f)) with a max of about 2 mol CO_2 m^{-2} yr^{-1} in GISSER and about 6 mol CO_2 - m^{-2} yr^{-1} in GISSEH. This elevated uptake in the GISSEH Southern Ocean compared to GISSER relates to the higher surface pCO_2 in GISSEH (by about 50 ppmv) than in GISSER (Fig. 9(c) and (d)) de-spite the warmer SSTs and the weaker surface winds in GISSEH.

At the equator, the Eastern Pacific source of CO_2 is more pro-nounced in the GISSER model than the GISSEH during both seasons (Fig. 8) due to greater pCO_2 and stronger trade winds (Fig. 2). Both these effects overpower the significantly warmer SST in the GISSER model, particularly along the equator. Elsewhere in the tropics, such as in the Warm Pool region, GISSEH pCO_2 is much higher than the atmospheric value (285.2 ppmv; Fig. 9) and therefore the out-gassing is more extensive. Here, the very high values of pCO_2 are related to the very low salinities (Fig. 5).

Annually, the Southern Hemisphere (south of 20°S) emits about 0.11 Pg Cyr^{-1} in GISSER and 0.37 Pg Cyr^{-1} in the GISSEH. Compared to the Takahashi atlas (Takahashi et al., 2009) in which the same region uptakes about 0.08 Pg Cyr^{-1}, the larger and opposite sign
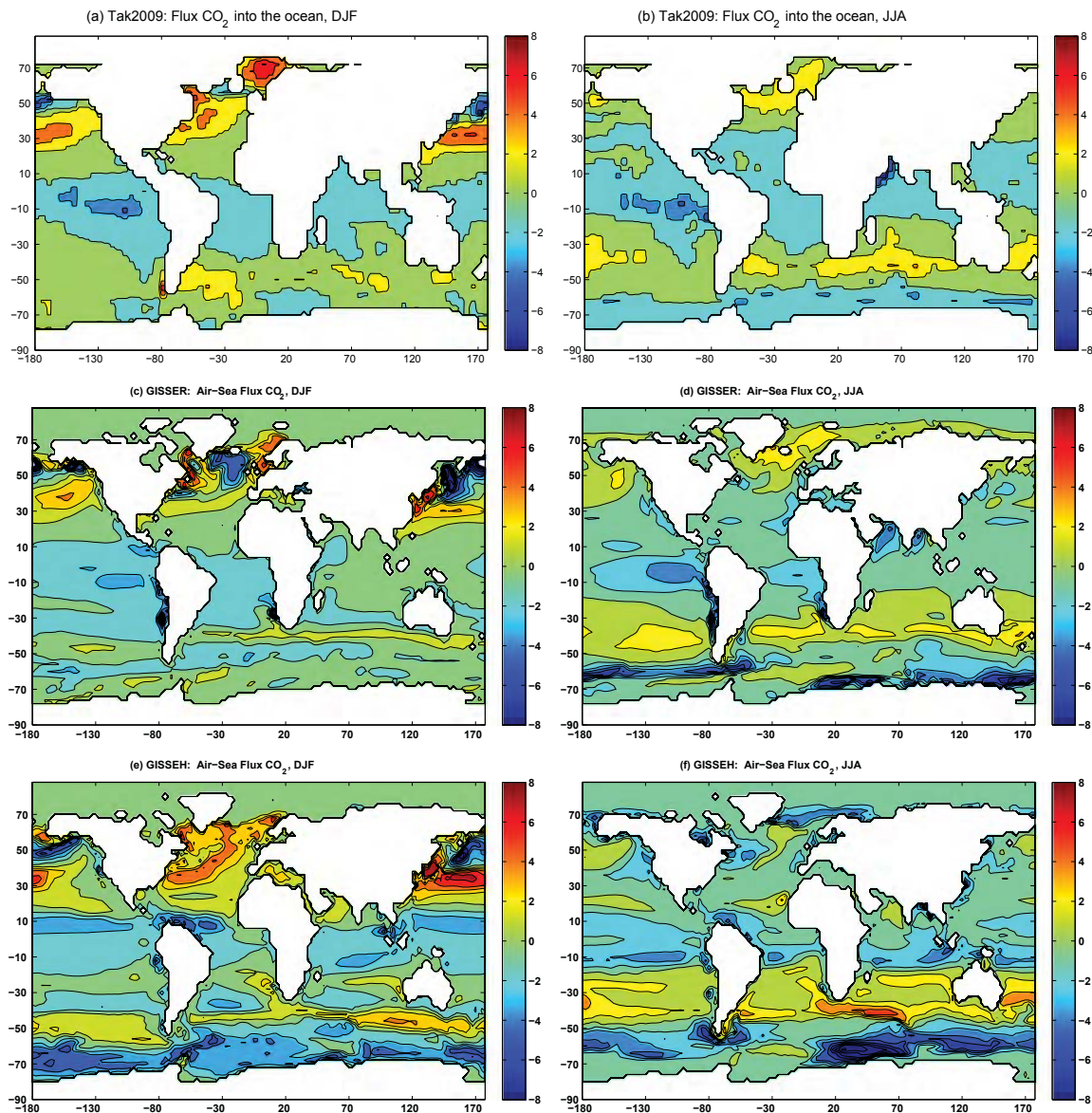

Fig. 8. Flux of CO_2 into the ocean (mol·CO_2 m^{-2} yr^{-1}) in the (a) and (b) Takahashi 2009 atlas, (c) and (d) GISSER and (e) and (f) GISSEH models for DJF (left panels) and JJA (right panels). Positive flux denotes ocean uptake.

flux in the GISS models is attributed to the larger disequilibrium of pCO_2 in the preindustrial climate that is modeled here than in the present climate (and hence the Takahashi atlas). In the equatorial regions GISS models predict a source of about 1.31 Pg Cyr^{-1} in the GISSER and 1.01 Pg Cyr^{-1} in the GISSEH. The equatorial source in the Takahashi atlas is 0.69 Pg Cyr^{-1} again due to the lower atmospheric concentrations of CO_2 in the model climate. The Northern Hemisphere oceans uptake about 0.45 Pg Cyr^{-1} in the GISSER and

0.46 Pg Cyr^{-1} in the GISSEH annually, whereas in Takahashi the uptake is estimated at 1.3 Pg Cyr^{-1}.

The geographical patterns of the natural CO_2 flux into the ocean compare well, both qualitatively and quantitatively, with inverse estimates from about 10 natural carbon cycle models as described in Mikaloff-Fletcher et al. (2007). Fig. 10 shows the GISSER and GISSEH flux integrals over several geographic regions as well as the multi-model mean and standard deviation from the inverse esti-
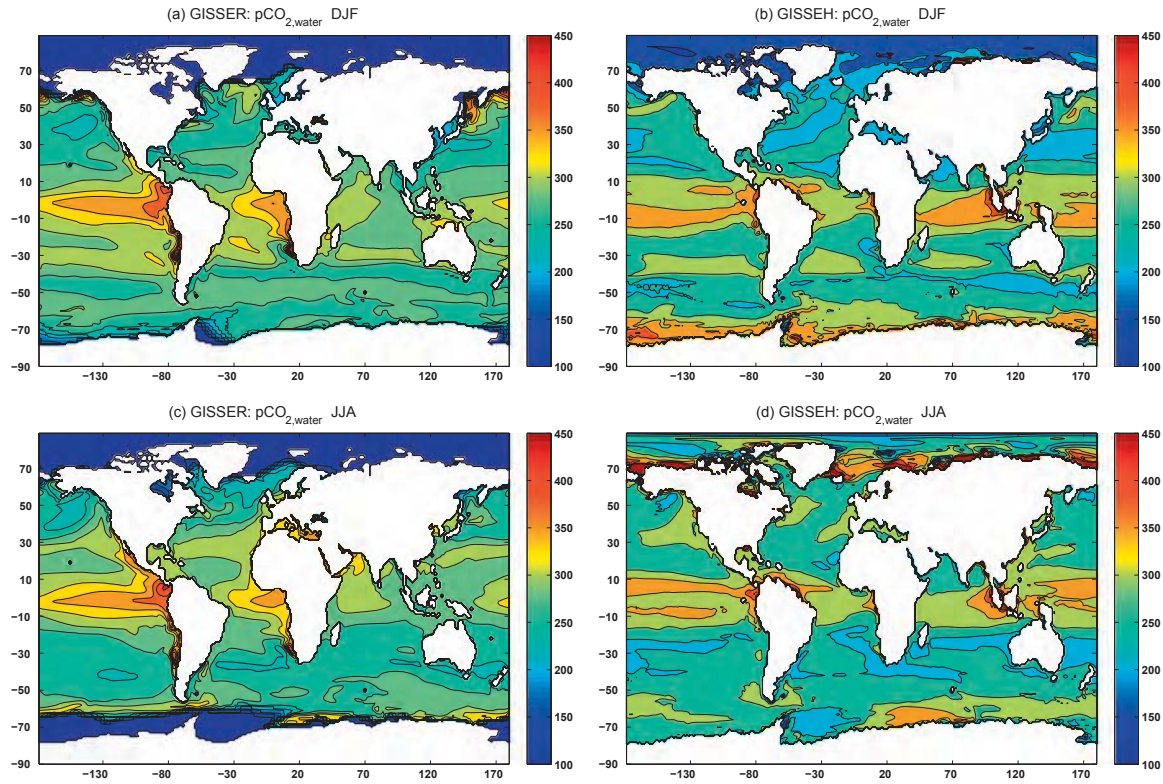

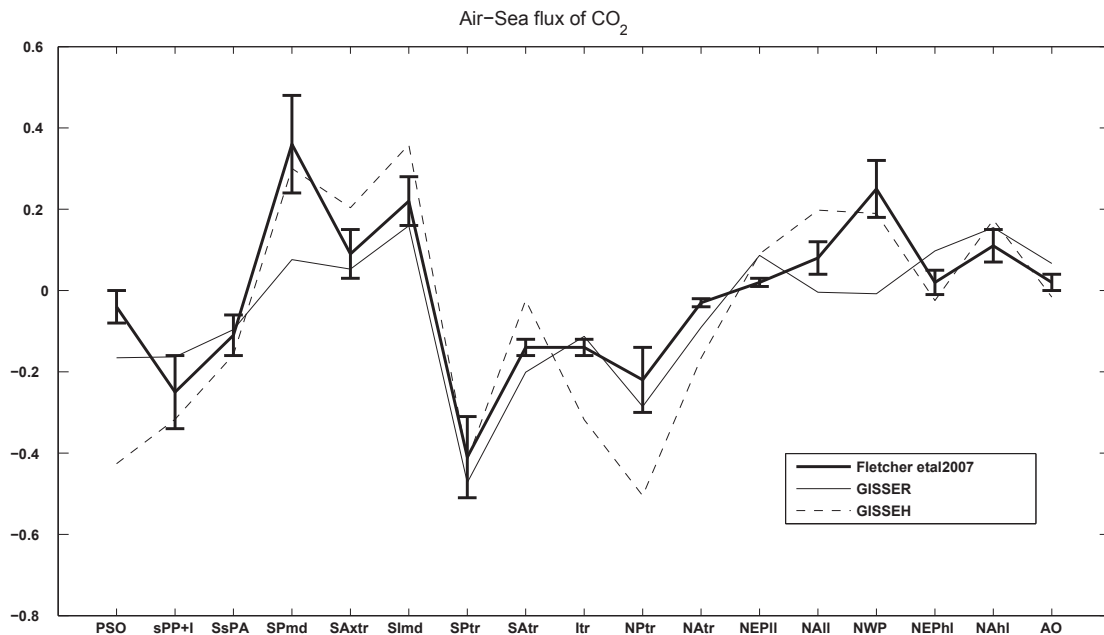**Fig. 9.** p·CO_2 distributions (in uatm) in GISSER and GISSEH for DJF and JJA.

Fig. 10. CO_2 flux (in Pg·Cyr^{-1}) into the ocean integrated over different regions, as in Mikaloff-Fletcher et al. (2007).
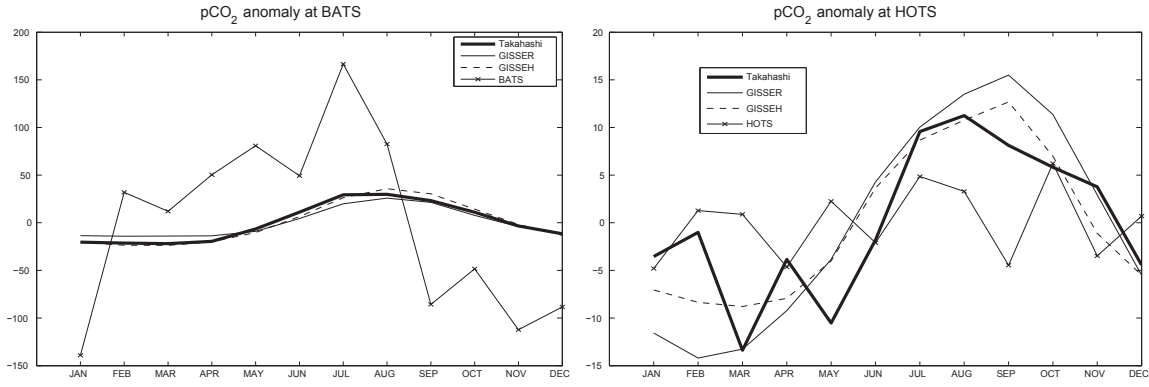
Fig. 11. pCO$_2$ values from observations, the Takahashi atlas and GISSER and GISSEH models at the locations of the Bermuda Atlantic Timeseries Study area (BATS) and the Hawaii Ocean Timeseries Study (HOTS).
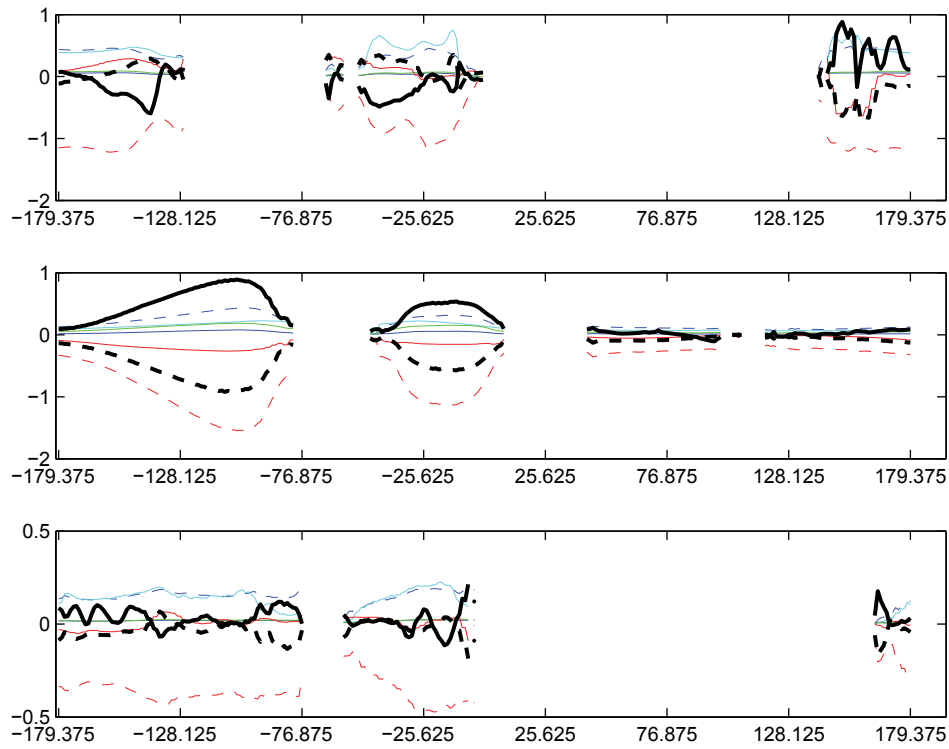

Fig. 12. Longitudinal variation of the depth integrated DIC tendencies (mmol C m^{-2} h^{-1}) as described by different terms in Eqn. 5 in GISSER only, along lines of constant latitude (top) 50° N, (middle) the equator, and (bottom) 70° S. Solid blue lines represent phytoplankton respiration, dashed blue lines represent remineralization, cyan lines bacterial degradation of DOC, green lines zooplankton respiration, solid red lines show gas exchange, and dashed red lines show phytoplankton growth. Dashed black lines are the sum of these biology terms and solid black lines show advection (mean + eddy). Note vertical axes range is different in the three panels.

mates. Both GISS models predict the natural CO$_2$ flux within the uncertainty range of the multi-model mean in most regions of the globe. Most notably, both GISS models fall outside the uncertainty ranges in the polar Southern Ocean where as Mikaloff-Fletcher et al. (2007) discuss even inverse model estimates are highly uncertain, and in the Arctic Ocean and the North Atlantic tropics.

In situ data in stations HOTS and BATS provide a useful tool assessing the quality of the modeled seasonal cycle of CO$_2$. Significant difficulty arises, however, when one tries to compare modeled fields which are smooth functions over a gridsize area (here about 100 km) with point measurements. Nevertheless, Fig. 11 shows that both GISS models capture the phase and magnitude

of the seasonal cycle exhibited in the Takahashi atlas, but underestimate its magnitude significantly at these locations.

Surface ocean pCO$_2$ biases reflect the DIC differences over most regions which will be discussed next.

4.3. The air–sea CO$_2$ flux: biological pump differences

DIC changes in the ocean are due to the air–sea flux of CO$_2$, metabolic processes, vertical mixing and lateral eddy diffusion (Gregg and Casey, 2007):

$$\frac{\partial}{\partial t}[DIC] = \nabla \cdot (K\nabla[DIC]) - \mathbf{V} \cdot \mathbf{V}[DIC] - \Phi\Sigma_i\mu_i P_i + \Phi\Omega\Sigma_i\mu_i P_i \quad (4)$$

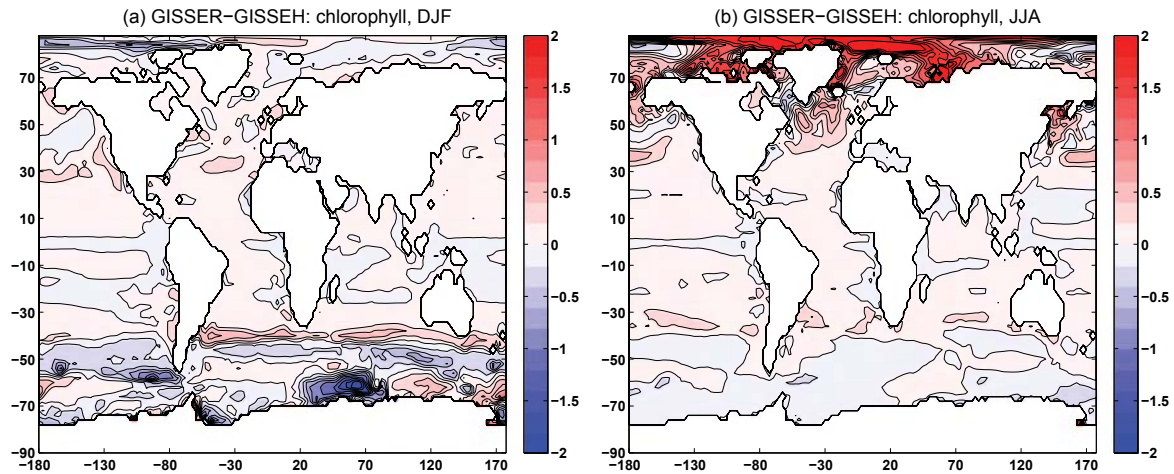$$+ \Phi\Theta H + \phi[DOC] + R\alpha_N D_C/(C:N) + F_{CO_2} \quad (5)$$

Fig. 13. Total chlorophyl concentration in mg chl/m³ differences in the two models (GISSER-GISSEH) for (a) DJF and (b) JJA.
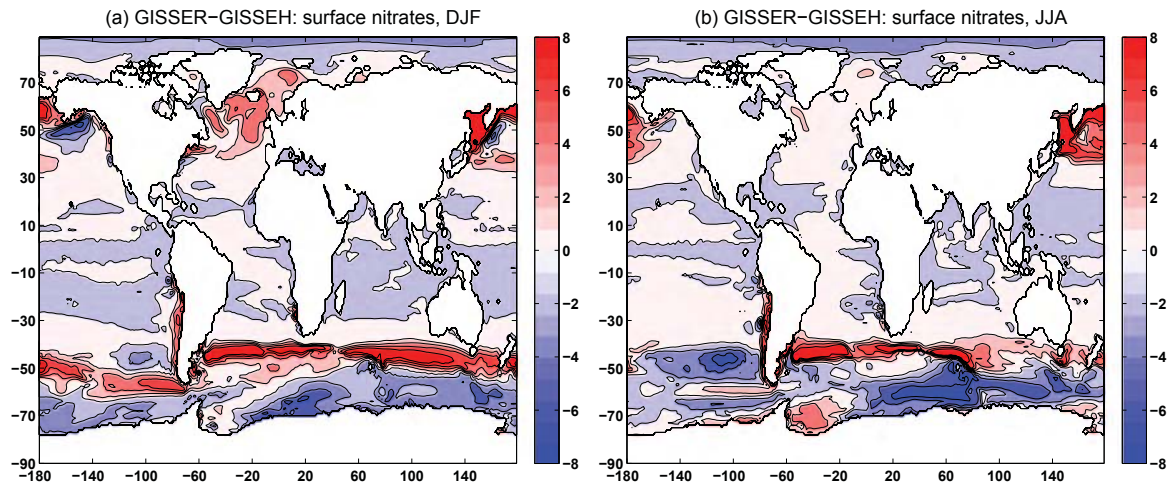

Fig. 14. Nitrates (in mmol N m⁻³) for (a) DJF and (b) JJA. Contour intervals are 2 mmol N m⁻³.

Table 2
Vector sinking rate of phytoplankton and carbon detritus at 31 °C, in m d⁻¹ (Gregg et al., 2012).

	Sinking rate (m d⁻¹)
Diatoms	0.75
Chlorophytes	0.25
Cyanobacteria	0.0085
Coccolithophores	0.3–1.4
Carbon detritus	40

Table 3
Regional correlations between modeled and observed annual climatologies of total chlorophyll (tchl), diatoms (diat), chlorophytes (chlo), coccolithophores (cocc), nitrate (nitr), silicate (sili), iron and DIC in the two models.

	tchl	diat	chlo	cyan	cocc	nitr	sili	iron	dic
GISSER	0.64	0.78	0.86	0.77	0.39	0.98	0.36	0.25	0.84
GISSEH	0.52	0.75	0.86	0.59	0.74	0.97	0.61	0.18	0.50

where the first term on the right-hand-side is the diffusion of DIC (turbulent mixing) in which K is parameterized based on Large et al., 1994. The second term is horizontal advection which includes eddy transport, followed in turn by phytoplankton (P_i) growth and respiration, zooplankton (H) respiration, bacterial degradation of

dissolved organic carbon (DOC), remineralization of detrital carbon and finally, F_{CO_2}, the flux due to gas exchange between the ocean and the atmosphere.

Fig. 12 (top panel) shows that gas exchange (solid red line) along 50°N is the leading term in the DIC changes in the North Atlantic deep convection region (longitudes: −70E to −40E) where intense CO_2 uptake occurs. Everywhere else at that latitude, chlorophyll growth (dashed red line) dominates all other terms in the DIC equation. Along the equator, phytoplankton growth (dashed red line) becomes the main driver for DIC decreases, and is further reinforced by outgassing. Similarly in the Southern Ocean, near the Antarctic coast (70°S), phytoplankton growth is the main sink of DIC. Horizontal advection (sum of the mean advection and the eddy stirring term) is of the same order of magnitude, opposite sign as the total biology terms nearly balancing the local DIC changes as expected from Eq. (5).

The biologically mediated DIC uptake is larger in GISSER because total chlorophyll is higher in this model over most regions except in the Southern Ocean south of about 50°S (Fig. 13). The geographical pattern is similar during both DJF and JJA although the differences are more pronounced during the warm season (DJF in the Southern Ocean; JJA in the Arctic).

During DJF, in North Atlantic higher chlorophyll distributions in GISSER (Fig. 13(a)) are sustained by increased nitrate load (Fig. 14(a)) which is due to deeper mixing there (Fig. 7), despite

the significantly colder SSTs (Fig. 3). On the contrary, the JJA blooms in the Arctic (Fig. 13(b)) are related to the increased warming of the water column (Fig. 3) as more ice melts in GISSER than in GISSEH.

In the tropical regions, over a narrow latitude band around the equator, GISSER has lower chlorophyl concentrations during both seasons, due to the colder SSTs as well as lower concentrations of nitrates (Fig. 14(a) and (b)).

In the Southern Ocean, south of 50°S particularly during DJF (the austral summer) chlorophyll is lower in GISSER because of lower nitrate load (Fig. 14(a)) in this model. Shallower mixed layers (Fig. 7) result mixing that does not extend deep enough to bring more nutrients to the surface.

In the Antarctic convergence zone (around 45°–50°S) increased biological production in GISSER is associated to the abundant nitrates there, due again to deeper MLD even though SST is colder. This is the area, the Subantarctic Front, where the Subantarctic Mode waters form, that is characterized by high nitrate and low silicate load and increased productivity. Surface waters in this region originate from the deep North Atlantic and are rich in remineralized nutrients.

Correlations between observed and modeled climatologies in each region (Table 3) reveal that GISSER has better skill in simulating ocean productivity and main phytoplankton groups than GISSEH. GISSER, and less so GISSEH, captures total chlorophyll and nitrate spatial patterns with high fidelity however, coccolithophores and silicate/iron distributions are not very realistic.

Deep carbon storage and export can be assessed through the model DIC biases. The annual-mean, zonal distributions of DIC in the two models are shown in Fig. 15. Surface DIC is lower in the equatorial regions in GISSER because of the more vigorous outgassing (Fig. 8). In the Northern Hemisphere subpolar regions, again, surface DIC is lower in the GISSER model because of biological uptake since there are extensive chlorophyll blooms there throughout the year (Fig. 13). In the Southern Ocean, however, surface DIC is higher in GISSER due to more intense mixing with deeper waters that are richer in DIC (Fig. 15) whereas the GISSEH sharp carbocline prevents such mixing. As a result, deep DIC distributions are higher in the GISSEH model (Fig. 16).

Comparison of the deep DIC distributions in the two models with the initial conditions (GLODAP) (Fig. 16) shows that at 1500 m GISSEH holds more DIC than GISSER and both models have
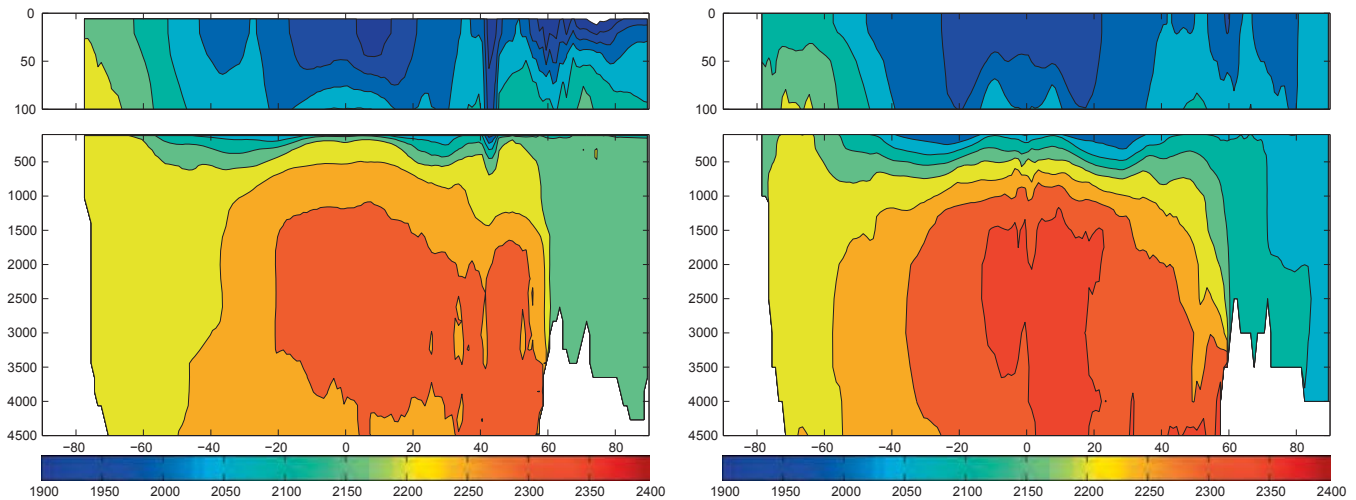

Fig. 15. Zonally averaged annual mean DIC in mmol C m^{-3}. On the left are distributions from GISSER and on the right from GISSEH.
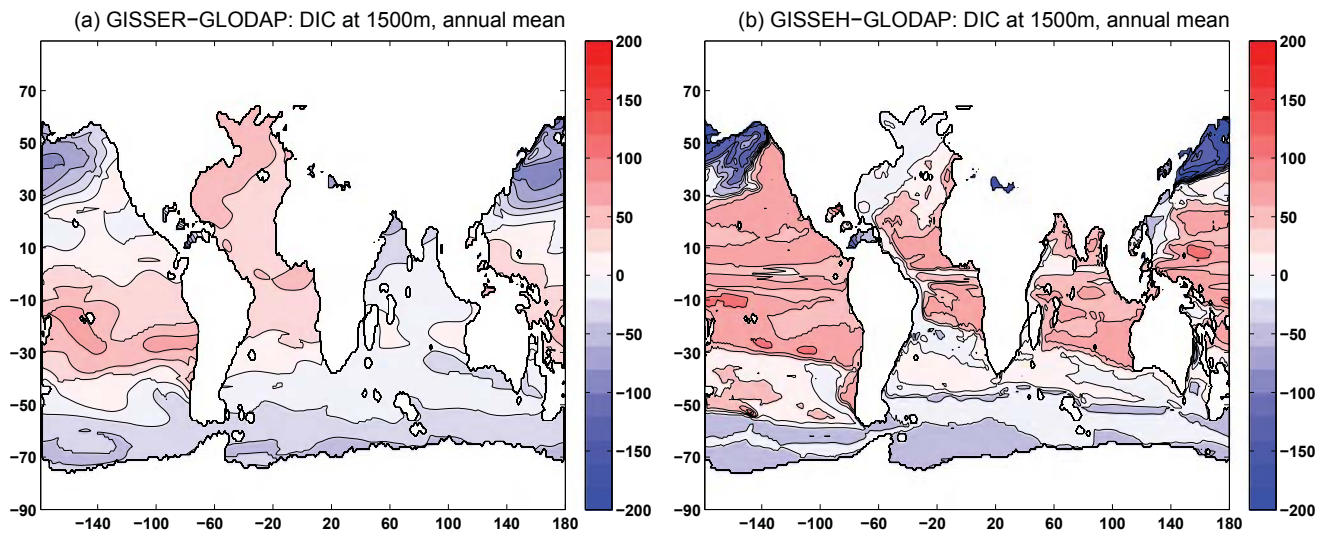

Fig. 16. DIC differences between the models and the GLODAP estimates at 1500 m. (a) GISSER-GLODAP and (b) GISSEH-GLODAP. Units are in mmol C m^{-3}.
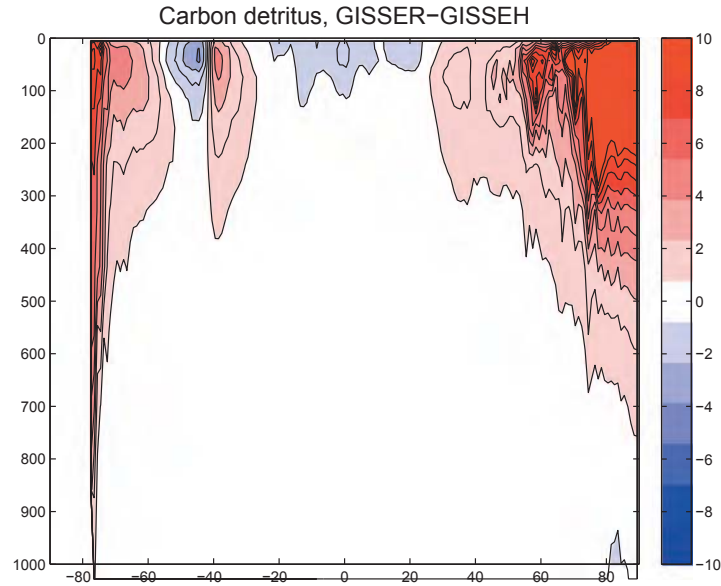
Fig. 17. Difference in particulate organic carbon (detritus) in the two model runs. Units are in mili-gr,C m^{-3}.
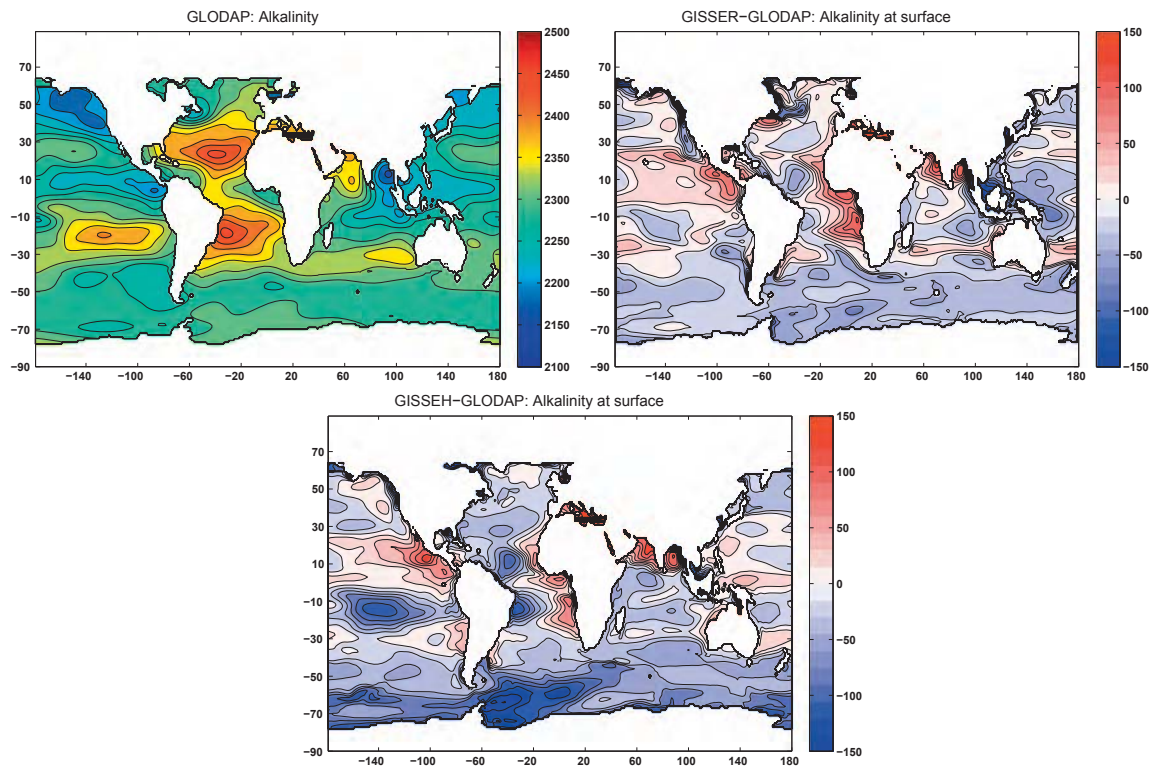

Fig. 18. Alkalinity climatology and model differences. (a) Alkalinity from GLODAP, (b) GISSER-GLODAP and (c) GISSEH-GLODAP.

more DIC than GLODAP particularly in low latitudes. Those patterns are explained by the more vigorous uptake in GISSEH and the higher productivity in GISSER in the North Atlantic convection region. Both models show depletion of DIC in the deep Southern Ocean regions, due to the intense outgassing and the deep mixing in these regions in both models, especially in HYCOM.

In addition to ventilation from the surface, another source for DIC at depth is the remineralization of the carbon detritus. GISSER has more detritus over most extratropics (Fig. 17) because of colder temperatures (Fig. 4) and less efficient remineralization there (Eq. (5)). Conversely, at low latitudes GISSER is warmer which implies

increased remineralization rates and leads to lower detritus concentrations. As a result, the globally integrated carbon export at 75 m is about 6.7 Pg Cyr^{-1} in GISSER and about 2 Pg Cyr^{-1} in GISSEH. In addition to weaker remineralization in GISSEH, other reasons for the decreased carbon export in GISSEH are the lower chlorophyl concentrations, the decreased vertical mixing and the subsequent lower surface DIC concentrations, as well as the more intense outgassing.

Since primary productivity is about 17 Pg Cyr^{-1} in GISSER and 2 Pg Cyr^{-1} in GISSEH, the carbon export efficiency, defined as the ratio of the globally integrated export and the globally integrated

primary productivity are very similar; 0.4 for GISSER and 0.3 for HYCOM.

4.4. The air–sea surface CO_2 flux: carbonate pump differences

The air–sea flux differences between the two models are strongly correlated with the pCO_2 differences, as discussed in Section 4.1. In addition to DIC, SST, SSS and surface nutrient distributions discussed previously, alkalinity also affects the DIC budget via the air–sea gas exchange. Theoretically, alkalinity changes with precipitation and evaporation as well as the production and dissolution of calcium carbonate, $CaCO_3$, and the assimilation and release of dissolved inorganic nitrogen. However, in the present model formulation, alkalinity is a constant and uniform function of salinity, and does not affect pCO_2 except only at the surface ocean where it is involved in gas exchange. Therefore, salinity biases discussed before (Fig. 5) reflect large underestimates of alkalinity in the Southern Ocean mainly (Fig. 18), which are more pronounced in the GISSEH model. In the North Atlantic, alkalinity biases are such that they explain the lower CO_2 uptake in the GISSER model during DJF whereas in the Southern Ocean alkalinity biases lead to more outgassing in the GISSEH. Compared to GLODAP estimates, model alkalinity is overpredicted in the upwelling coastal regions but is underestimated everywhere else, particularly in the Southern Ocean. This implies that in this region the excessive model outgassing compared to Takahashi (Fig. 8), cannot be explained by the alkalinity biases there.

5. Conclusions

This paper documents the similarities, differences and possible driving mechanisms of the natural carbon cycle between the two NASA-GISS climate models. These two climate models share the same atmospheric, land, ice and ocean carbon components but differ in the ocean physics component. The ocean models employ different vertical coordinate system which is known to produce different distributions of seawater properties at depths where numerical and spurious diapycnal mixing can become important (Bleck et al., 1992; Griffies et al., 2000). Moreover, the ocean models differ in the details of the vertical mixing scheme (KPP); in GISSER KPP extends to the bottom of the water column but non-local terms are not included whereas in GISSEH it only reaches the bottom of the mixed layer. Eddy mixing along isopycnals (Gent and McWilliams, 1990) is only explicitly modeled in GISSER, whereas in GISSEH is approximated by isopycnal thickness diffusion for the regions where these isopycnals do not outcrop. Moreover, there is no tracer horizontal advection in GISSEH. Although the models are different in other ways, the significantly decreased vertical diffusion/mixing below the mixed layer in the GISSEH is perhaps the main difference between them.

Model results, even though they refer to an unperturbed, stable preindustrial physical climate, are assessed against observations from present day climate, in order to estimate how large inter-model differences are compared to the anthropogenic signal, thereby setting the stage for present-day GISS model evaluations.

We find that model differences in the natural CO_2 flux are explained by differences in surface temperature, salinities and winds, which are in turn controlled by the different distributions of clouds and ice cover in the two models as well as processes in the interior of the ocean. We conclude that the air–sea flux is most sensitive to differences in the strength of the surface winds in the two models and the differences in the partial CO_2 distributions, in general agreement with Doney et al. (2004, 2006).

Storm-track winds in the North Atlantic are stronger in the GISSEH model, due to stronger evaporative feedbacks driven by the

warmer SSTs. Lower vertical, interior ocean mixing in GISSEH, though, which is an inherent feature of layer models, overwhelms the wind effect, slowing down the thermohaline circulation in the model, resulting in global northern hemisphere meridional overturning circulation (MOC) of about 18 Sv as opposed to 25 Sv in GISSER. Deep convection in GISSEH reaches shallower depths than GISSER and therefore brings to the surface lower amounts of DIC and nutrients. Total chlorophyll and primary productivity are therefore larger in GISSER in the North Atlantic due to more nutrients. Therefore the more intense uptake in HYCOM is solubility driven (winds, pCO_2) rather than biologically driven (primary production).

In the tropics, stronger outgassing in the GISSER model, particularly in the eastern equatorial Pacific, is attributed to higher surface temperatures but also stronger trade winds in this model. Still, equatorial upwelling and outgassing is reduced in GISSER compared to observations (Takahashi atlas) due to weaker than observed trade winds. This is a complex model deficiency compounded by the lack of horizontal resolution in the Russell ocean model which therefore does not resolve the equatorial waveguide and the associated baroclinic instabilities. However, other differences between the ocean models, such as horizontal advection and eddy stirring are important in this region and are modeled differently in the two models.

The Southern Ocean is a region where the large scale winds through Ekman layer dynamics subduct most of the carbon dioxide that enters the ocean (Ito et al., 2010) while eddies, which are responsible for the lateral transport through eddy stirring, play a lesser role. We find that the models' Southern Ocean fluxes are of considerably different magnitude and/or sign from the Takahashi atlas, and that these differences cannot be explained by alkalinity, SSTs or surface winds. Both models cannot resolve adequately lateral eddy mixing resulting in mixed layer depths with are too shallow in this region, especially in GISSEH, leading to unrealistic subduction processes. Moreover, the particularly shallow mixed layer depths in HYCOM are a result of the higher SSTs and the positive SST-MLD feedback in which shallower mixed layers lead to more heating of the surface layer, thereby increasing the static stability of the water column and further reducing vertical mixing. The higher SSTs affect gas exchange not through solubility but rather through the shallow and sharper thermocline and the reduced exchanges of DIC and nutrients with the deeper ocean.

In the Southern Ocean two distinct regions emerge: north of 50°S, i.e. roughly north of the divergence zone, where the GISSEH ocean surface is warmer and slightly more saline, winds are weaker (especially during DJF), pCO_2 is greater, total chlorophyll and nutrients are lower particularly along the Subantarctic Convergence Zone and south of 50°S, where the GISSER ocean model outgasses less, is warmer and more saline at the surface, winds are weaker total chlorophyll and nutrients are lower. In the GISSER model the Antarctic Bottom Water (ABW) forms near the Antarctic coast and unrealistic mixing processes at depth in GISSER result in the fast depletion of ABW. The area between SAZ and the divergence zone is very sensitive to parameterizations of vertical mixing and as well as the isopycnal diffusion mixing (Gent–McWilliams) and since these are modeled differently in our two ocean models, this region emerges as the most sensitive to ocean model parameterizations. This is in agreement with the idea that excessive Southern Ocean mixing (vertical diffusion or eddy stirring) and/or weaker winds (as they are in both models here, especially GISSER), the dominant transformation of abyssal waters into light water takes place within the low-latitude pycnocline instead of in the Southern Ocean (Gnanadesikan et al., 2002). Such a regional difference greatly affects the Southern Ocean sink of CO_2 in both models, particularly in GISSER. Nevertheless, the Southern Ocean

region is one of highly uncertain estimates of the CO_2 gas exchange in several other models, as shown in Mikaloff-Fletcher et al. (2007).

GISSER has better skill in simulating the biological pump than GISSEH. Very little mixing between the upper ocean and the interior brings less nutrients to the surface reducing the biological production in GISSEH. GISSER, and less so GISSEH, captures total chlorophyll and nitrate spatial patterns with high fidelity however, coccolithophores and silicate/iron distributions are not very realistic. The lack of processes such as denitrification and the highly approximate alkalinity balance in both models are probably responsible for these biases.

The two models tend to have the largest DIC values at mid-depths, along the NADW pathway. Therefore, GISSEH which is characterized by reduced interior mixing, is colder and holds more DIC there at these depths. In the Southern Ocean, both models have lower DIC than GLODAP due to deeper mixing and large outgassing there.

Both models have lower than observed primary productivity and carbon export, despite the fact that they simulate fairly well total chlorophyl concentrations, which is a shared deficiency among other models (Carr et al., 2006). We are presently investigating the sensitivity of the carbon cycle model (NOBM) to remineralization and sinking parameterizations. GISSEH exhibits particularly reduced primary productivity and export compared to GISSER both of which result from a combination of factors such as the lower chlorophyl concentrations, the decreased vertical mixing and the subsequently reduced surface DIC and nutrients concentrations. Carbon export efficiency though, which is a measure of the strength of the biological pump, is similar in the two models, since the same processes which are responsible for keeping primary productivity low are also responsible for keeping carbon export low.

To conclude, physical ocean model differences which feed into atmospheric fields, such as the storm track strength, evaporation and precipitation and net heating over the ocean, result in solubility and hence uptake differences in the two models. Vertical mixing differences are mostly responsible for the divergent model responses with regards to the biological pump. Therefore the quality of the ocean component is critical for the realistic representation of the natural CO_2 ocean sink. Future studies will assess how the differences between the ocean model components might impact the sensitivity or the transient behavior of the oceanic carbon cycle in the GISS climate models.

Acknowledgements

References

Antonov, J.I., Locarnini, R.A., Boyer, T.P., Mishonov, A.V., Garcia, H.E., 2006. World ocean atlas 2005, vol. 2: Salinity. In: Levitus, S. (Ed.), NOAA Atlas NESDIS 62. US Government Printing Office, Washington, DC, p. 182.

Bleck, R., Rooth, C., Hu, D., Smith, L., 1992. Ventilation patterns and mode water formation in a wind- and thermodynamically driven isopycnic coordinate model of the North Atlantic. J. Phys. Oceanogr. 22, 1486G1505.

Bleck, R., Smith, L.T., 1990. A wind-driven isopycnic coordinate model some simulations because it removes marginally resolved of the north and equatorial atlantic ocean. 1. Model development gravity waves without affecting geostrophically balanced and supporting experiments. J. Geophys. Res. C 95.

Broecker, W., Peng, T., Ostlund, G., 1986. The distribution of bomb tritium in the ocean. J. Geophys. Res. 91, 14331–14344.

Carr, M., Friedrichs, M., Schmeltz, M., Aita, M.N., Antoine, D., Arrigo, K., Asanuma, I., Aumont, O., Barber, R., Behrenfeld, M., 2006. A comparison of global estimates of marine primary production from ocean color. Deep Sea Res. Part II: Topical Stud. Oceanogr. 53 (5–7), 741–770.

Cox, P., Betts, R., Jones, C., Spall, S., Totterdell, I., 2000. Acceleration of global warming due to carbon-cycle feedbacks in a coupled climate model. Nature 408, 184–187.

Csanady, G., 1986. Mass transfer to and from small particles in the sea. Limnol. Oceanogr. 31, 237–248.

deBoyer Montégut, C., Madec, G., Fischer, A.S., Lazar, A., Iudicone, D., 2004. Mixed layer depth over the global ocean: an examination of profile data and a profile-based climatology. J. Geophys. Res. 109.

Doney, S., Lindsay, K., Caldeira, K., Campin, J., Drange, H., Dutay, J., Follows, M., Gao, Y., Gnanadesikan, A., Gruber, N., 2004. Evaluating global ocean carbon models: the importance of realistic physics. Global Biogeochem. Cycles 18 (3).

Doney, S., Lindsay, K., Fung, I., John, J., 2006. Natural variability in a stable, 1000-year global coupled climate-carbon cycle simulation. J. Climate 19.

Dore, J., Lukas, R., Sadler, D., Church, M., Karl, D., 2009. Physical and biogeochemical modulation of ocean acidification in the central north pacific. Proc. Natl. Acad. Sci. 106, 12235–12240.

Friedlingstein, P., Cox, P., Betts, R., Bopp, L., von Bloh, W., Brovkin, V., Cadule, P., Doney, S., Eby, M., Fung, I., Bala, G., John, J., Jones, C., Joos, F., Kato, T., Kawamiya, M., Knorr, W., Lindsay, K., Matthews, H.D., Raddatz, T., Rayner, P., Reick, C., Roeckner, E., Schnitzler, K.-G., Schnur, R., Strassmann, K., Weaver, A.J., Yoshikawa, C., Zeng, N., 2006. Climatecarbon cycle feedback analysis: Results from the c4mip model intercomparison. J. Clim. 19, 3337–3353.

Fung, I.Y., Meyn, S.K., Tegen, I., Doney, S.C., John, J.G., Bishop, J.K.B., 2000. Iron supply and demand in the upper ocean. Global Biogeochem. Cycles 14 (1), 281–295.

Garcia, H.E., Locarnini, R.A., Boyer, T.P., Antonov, J.I., 2006. World ocean atlas 2005, vol. 4: Nutrients (phosphate, nitrate, silicate). In: Levitus, S. (Ed.), NOAA Atlas NESDIS 64. US Government Printing Office, Washington, DC, p. 396.

Gargett, A., 1984. Vertical eddy diffusivity in the ocean interior. J. Mar. Res. 42 (2), 359–393.

Gent, P., McWilliams, J., 1990. Isopycnal mixing in ocean circulation models. J. Phys. Oceanogr. 20, 1–6.

Ginoux, P., Chin, M., Tegen, I., Prospero, J., Holben, B., Dubovik, O., Lin, S.-J., 2001. Sources and distributions of dust aerosols simulated with the gocart model. Biogeochem. Cycles 16.

Gnanadesikan, A., Slater, R., Gruber, N., Sarmiento, J.L., 2002. Oceanic vertical exchange and new production: a comparison between models and observations. Deep Sea Res. – Part II 49, 363–401.

Gregg, W., Casey, N., 2009. Skill assessment of a spectral ocean-atmosphere radiative model. J. Mar. Syst. 76 (1–2), 49–63.

Gregg, W., Casey, N., Rousseaux, C., 2012. Global surface ocean carbon estimates in a model forced by Merra. NASA Technical Report Series on Global Modeling and Data Assimilation, vol. 31, 30pp.

Gregg, W., Casey, N.W., 2007. Modeling coccolithophores in the global oceans. Deep-Sea Res. II 54.

Gregg, W., Conkright, M.E., Ginoux, P., O'Reilly, J.E., Casey, N.W., 2003a. Ocean primary production and climate: global decadal changes. Geophys. Res. Lett. 30 (15), 1809.

Gregg, W., Ginoux, P., Schopf, P., Casey, N., 2003b. Phytoplankton and iron: validation of a global three-dimensional ocean biogeochemical model. Deep Sea Res. Part II: Topical Stud. Oceanogr. 50 (22–26), 3143–3169.

Gregg, W.W., Conkright, M.E., 2002. Decadal changes in global ocean chlorophyll. Geophys. Res. Lett. 29 (15).

Griffies, S.M., Pacanowski, R., Hallberg, R.R., 2000. Spurious diapycnal mixing associated with advection in a z-coordinate ocean model. Mon. Weather Rev. 128, 538–564.

Gruber, N., Gloor, M., Fletcher, S., Doney, S., Dutkiewicz, S., Follows, M., Gerber, M., Jacobson, A., Joos, F., Lindsay, K., 2009. Oceanic sources, sinks, and transport of atmospheric CO_2. Global Biogeochem. Cycles 23, 1601–1622.

Hansen, J., Sato, Mki., Ruedy, R., Kharecha, P., Lacis, A., Miller, R.L., Nazarenko, L., Lo, K., Schmidt, G.A., Russell, G., Aleinov, I., Bauer, S., Baum, E., Cairns, B., Canuto, V., Chandler, M., Cheng, Y., Cohen, A., Del Genio, A., Faluvegi, G., Fleming, E., Friend, A., Hall, T., Jackman, C., Jonas, J., Kelley, M., Kiang, N.Y., Koch, D., Labow, G., Lerner, J., Menon, S., Novakov, T., Oinas, V., Perlwitz, Ja., Perlwitz, Ju., Rind, D., Romanou, A., Schmunk, R., Shindell, D., Stone, P., Sun, S., Streets, D., Tausnev, N., Thresher, D., Unger, N., Yao, M., Zhang, S., 2007. Climate simulations for 1880–2003 with GISS Model. E. Clim. Dynam. 29, 661–696.

Henson, S.A., Sanders, R., Madsen, E., 2012. Global patterns in efficiency of particulate organic carbon export and transfer to the deep ocean. Global Biogeochem. Cycles 26.

Ito, T., Woloszyn, M., Mazloff, M., 2010. Anthropogenic carbon dioxide transport in the Southern Ocean driven by Ekman flow. Nature 463 (7277), 80–83.

Key, R., Kozyr, A., Sabine, C., Lee, K., Wanninkhof, R., Bullister, J., Feely, R., Millero, F., Mordy, C., Peng, T.-H., 2004. A global ocean carbon climatology: results from Glodap. Global Biogeochem. Cycles 18, GB4031.

Khatiwala, S., Primeau, F., Hall, T., 2009. Reconstruction of the history of anthropogenic CO_2 concentrations in the ocean. Nature 462, 346–349.

Large, W., McWilliams, J., Doney, S., 1994. Oceanic vertical mixing: a review and a model with a nonlocal boundary layer parameterization. Rev. Geophys. 32 (4), 363–401.

LeQuéré, C., Raupach, M.R., Canadell, J.G., Marland, G., Bopp, L., Ciais, P., Conway, T.J., Doney, S.C., Feely, R.A., Foster, P., Friedlingstein, P., Gurney, K., Houghton, R.A., House, J.I., Huntingford, C., Levy, P.E., Lomas, M.R., Majkut, J., Metzl, N., Ometto, J.P., Peters, G.P., Colin Prentice, I., Randerson, J.T., Running, S.W., Sarmiento, J.L., Schuster, U., Sitch, S., Takahashi, T., Viovy, N., van der Werf, G.R., Ian Woodward, F., 2009. Trends in the sources and sinks of carbon dioxide. Nat. Geosci. 2 (12), 831–836.

Locarnini, R.A., Mishonov, A.V., Antonov, J.I., Boyer, T.P., Garcia, H.E., 2006. World ocean atlas 2005, vol. 1: Temperature. In: Levitus, S. (Ed.), NOAA Atlas NESDIS 61. US Government Printing Office, Washington, DC, p. 182.

Marinov, I., Follows, M., Gnanadesikan, A., Sarmiento, J., Slater, R., 2008a. How does ocean biology affect atmospheric pCO_2? Theory and models. J. Geophys. Res. 113, C07032.

Marinov, I., Gnanadesikan, A., Sarmiento, J.L., Toggweiler, J.R., Follows, M., Mignone, B.K., 2008b. Impact of oceanic circulation on biological carbon storage in the ocean and atmospheric pCO_2. Global Geochem. Cycles 22, 1–15.

McDougall, T., Dewar, W., 1998. Vertical mixing, cabbeling and thermobaricity in layered models. J. Phys. Oceanogr. 28, 1458–1480.

Mikaloff-Fletcher, S., Gruber, N., Jacobson, A.R., Gloor, M., Doney, S.C., Dutkiewicz, S., Gerber, M., Follows, M., Joos, F., Lindsay, K., Menemenlis, D., Mouchet, A., Müller, S.A., Sarmiento, J.L., 2007. Inverse estimates of the oceanic sources and sinks of natural CO_2 and the implied oceanic carbon transport. Global Biogeochem. Cycles 21 (1), GB1010.

Prather, M.J., 1986. Numerical advection by conservation of second-order moments. J. Geophys. Res. 91 (D6), 6671–6681.

Russell, G., Miller, J., Rind, D., 1995. A coupled atmosphere–ocean model for transient climate change studies. Atmos. Ocean 33, 683–730.

Sabine, C., Feely, R., Gruber, N., Key, R., Lee, K., Bullister, J., Wanninkhof, R., Wong, C., Wallace, D., Tilbrook, B., Millero, F., Peng, T.-H., Kozyr, A., Ono, T., Rios, A., 2004. The oceanic sink for anthropogenic CO_2. Science 305, 367–371.

Schmidt, G.A., Ruedy, R., Hansen, J.E., Aleinov, I., Bell, N., Bauer, M., Bauer, S., Cairns, B., Canuto, V., Cheng, Y., Del Genio, A., Faluvegi, G., Friend, A.D., Hall, T.M., Hu, Y., Kelley, M., Kiang, N.Y., Koch, D., Lacis, A.A., Lerner, J., Lo, K.K., Miller, R.L., Nazarenko, L., Oinas, V., Perlwitz, J., Perlwitz, J., Rind, D., Romanou, A., Russell, G.L., Sato, M., Shindell, D.T., Stone, P.H., Sun, S., Tausnev, N., Thresher, D., Yao, M.-S., 2006. Present-day atmospheric simulations using GISS model: comparison to in situ, satellite, and reanalysis data. J. Clim.

Schmidt, G.A., Kelley, M., Nazarenko, L., Ruedy, R., Russell, G.L., Aleinov, I., Bauer, M., Bauer, S., Bhat, M. K., Bleck, R., Canuto, V., Chen, Y., Cheng, Y., Clune, T.L., DelGenio, A., de Fainchtein, R., Faluvegi, G., Hansen, J.E., Healy, R.J., Kiang, N.Y.,

Koch, D., Lacis, A.A., LeGrande, A.N., Lerner, J., Lo, K.K., Elaine, Mathews, E., Menon, S., Miller, R.L., Oinas, V., Oloso, A.O., Perlwitz, J., Puma, M.J., Putman, W.M., Rind, D., Romanou, A., Sato, M., Shindell, D.T., Sun, S., Syed, R.A. , Tausnev, N., Tsigaridis, K., Unger, N., Voulgarakis, A., Yao, M.-S., Zhang, J., 2012. Configuration and assessment of the GISS ModelE2 contributions to the CMIP5 archive. J. Climate. submitted for publication.

Schmidt, G.A., Coauthors, 2006. Present-day atmospheric simulations using GISS model E: comparison to in situ, satellite, and reanalysis data. J. Climate 19, 153–192.

Sun, S., Bleck, R., 2006. Geographic distribution of the diapycnal component of thermohaline circulations in coupled climate models. Ocean Modell. 15 (3-4), 177–199.

Takahashi, T., Sutherland, S.C., Wanninkhof, R., Sweeney, C., Feely, R.A., Chipman, D.W., Hales, B., Friederich, G., Chavez, F., Sabine, C., Watson, A., Bakker, D.C.E., Schuster, U., Metzl, N., Yoshikawa-Inoue, H., Ishii, M., Midorikawa, T., Nojiri, Y., Körtzinger, A., Steinhoff, T., Hoppema, M., Olafsson, J., Arnarson, T.S., Tilbrook, B., Johannessen, T., Olsen, A., Bellerby, R., Wong, C.S., Delille, B., Bates, N.R., de Baar, H.J.W., 2009. Climatological mean and decadal change in surface ocean pCO_2, and net sea-air CO_2 flux over the global oceans. Deep Sea Res. Part II, 554–577.

Takahashi, T., Sutherland, S., Wanninkhof, R., Sweeney, C., Feely, R., Chipman, D., Hales, B., Friederich, G., Chavez, F., Sabine, C., 2009. Climatological mean and decadal change in surface ocean pCO_2, and net sea–air CO_2 flux over the global oceans. Deep Sea Res. Part II: Topical Stud. Oceanogr. 56 (8–10), 554–577.

Volk, T., Hoffert, M.I., 1985. Ocean carbon pumps: analysis of relative strengths and efficiencies in ocean driven atmospheric CO_2 changes. In: Sundquist, E.T., Broecker, W.S. (Eds.), The Carbon Cycle and Atmospheric CO_2: Natural Variations Archaean to Present, Geophysical Monograph Series, vol. 32. AGU, Washington, DC, p. 99G110.

Wanninkhof, R., 1992. Relationship between wind speed and gas exchange over the ocean. J. Geophys. Res. 97 (C5), 7373–7382.

Yu, L., Jin, X., Weller, R.A., 2008. Multidecade global flux datasets from the objectively analyzed air–sea fluxes (oaflux) project: latent and sensible heat fluxes, ocean evaporation, and related surface meteorological variables. OAFlux Project Technical Report, OA-2008-01, 64pp.

Zhang, Y., Rossow, W., Lacis, A., Oinas, V., Mishchenko, M., 2004. Calculation of radiative fluxes from the surface to top of atmosphere based on ISCCP and other global data sets: refinements of the radiative transfer model and the input data. J. Geophys. Res. – Atmos. 109 (D19), D19105.